JGR Space Physics

RESEARCH ARTICLE
10.1029/2019JA026693

Characteristics of the Quiet-Time Hot Spot Gravity Waves Observed by GOCE Over the Southern Andes on 5 July 2010

Sharon L. Vadas[1], Shuang Xu[2,3], Jia Yue[2], Katrina Bossert[4], Erich Becker[5], and Gerd Baumgarten[5]

[1]Northwest Research Associates, Boulder, CO, USA, [2]Atmospheric and Planetary Sciences, Hampton University, Hampton, VA, USA, [3]School of Earth and Space Sciences, University of Science and Technology of China, Hefei, China, [4]Department of Electric and Computer Engineering, and Geophysical Institute, University of Alaska Fairbanks, Fairbanks, AK, USA, [5]Leibniz Institute of Atmospheric Physics, Kühlungsborn, Germany

This article is a companion to Vadas and Becker (2019), https://doi.org/10.1029/2019JA026694.

Key Points:
- The GW dissipative dispersion and polarization relations were used to uniquely characterize the hot spot GWs
- The hot spot GWs were medium to large scale, had periods <1 hr, and had horizontal intrinsic phase speeds c_{IH} = 245–630 m/s
- All of the hot spot GWs were likely secondary, tertiary, or higher-order GWs from MW breaking

Correspondence to:
S. L. Vadas,
vasha@nwra.com

Citation:
Vadas, S. L., Xu, S., Yue, J., Bossert, K., Becker, E., & Baumgarten, G. (2019). Characteristics of the quiet-time hot spot gravity waves observed by GOCE over the Southern Andes on 5 July 2010. *Journal of Geophysical Research: Space Physics*, *124*, 7034–7061. https://doi.org/10.1029/2019JA026693

Received 5 MAR 2019
Accepted 4 MAY 2019
Accepted article online 8 MAY 2019
Published online 14 AUG 2019

Abstract We analyze quiet-time data from the Gravity Field and Ocean Circulation Explorer satellite as it overpassed the Southern Andes at $z \simeq 275$ km on 5 July 2010 at 23 UT. We extract the 20 largest traveling atmospheric disturbances from the density perturbations and cross-track winds using Fourier analysis. Using gravity wave (GW) dissipative theory that includes realistic molecular viscosity, we search parameter space to determine which hot spot traveling atmospheric disturbances are GWs. This results in the identification of 17 GWs having horizontal wavelengths λ_H = 170–1,850 km, intrinsic periods τ_{Ir} = 11–54 min, intrinsic horizontal phase speeds c_{IH} = 245–630 m/s, and density perturbations $\rho'/\bar{\rho} \sim 0.03$–7%. We unambiguously determine the propagation direction for 11 of these GWs and find that most had large meridional components to their propagation directions. Using reverse ray tracing, we find that 10 of these GWs must have been created in the mesosphere or thermosphere. We show that mountain waves (MWs) were observed in the stratosphere earlier that day and that these MWs saturated at $z \sim$ 70–75 km from convective instability. We suggest that these 10 Gravity Field and Ocean Circulation Explorer hot spot GWs are likely tertiary (or higher-order) GWs created from the dissipation of secondary GWs excited by the local body forces created from MW breaking. We suggest that the other GW is likely a secondary or tertiary (or higher-order) GW. This study strongly suggests that the hot spot GWs over the Southern Andes in the quiet-time middle winter thermosphere cannot be successfully modeled by conventional global circulation models where GWs are parameterized and launched in the troposphere or stratosphere.

1. Introduction

1.1. MW Propagation and Breaking

Mountain waves (MWs) are created when wind flows over a mountain. If the wind is steady-state in time, then the MWs have ground-based phase speeds that are equal to zero. If the background wind is conducive to MW propagation, then a MW's amplitude grows exponentially in altitude because the background density decreases exponentially in altitude (Hines, 1960). Eventually, however, a MW's amplitude becomes too large, causing the MW to break from convective instability at the altitude where

$$\frac{|u'_H|}{|c_H - U_H|} \simeq 0.7 - 1.0 \tag{1}$$

(Fritts & Alexander, 2003; Lindzen, 1981). Here $u'_H = \sqrt{(u')^2 + (v')^2}$ is the horizontal wind perturbation of the MW, u' and v' are the zonal and meridional wind perturbations, $c_H = \omega_r/k_H$ is the ground-based horizontal phase speed, $\omega_r = 2\pi/\tau_r$ is the ground-based frequency, $k_H = \sqrt{k^2 + l^2} = 2\pi/\lambda_H$, λ_H is the horizontal wavelength, k, l, and m are the zonal, meridional, and vertical wave numbers, respectively,

$$U_H = (k\bar{U} + l\bar{V})/k_H \tag{2}$$

is the background horizontal wind along the direction of MW propagation, and $\bar{U}$ and $\bar{V}$ are the zonal and meridional components of the background wind, respectively. Wintertime MW breaking from convective

instability typically occurs in the stratosphere, although it can occur in the mesosphere if the MW's initial amplitude is small (Bossert et al., 2015, 2017; Fritts et al., 2016; Heale et al., 2017; Eckermann et al., 2016).

A MW also breaks as it approaches a critical level. A critical level occurs when the background wind projected along the MW's propagation direction reverses direction (e.g., goes from eastward to westward, or vice versa, for a zonally propagating MW), which causes the MW's vertical wavelength, λ_z, to decrease rapidly to zero. This decrease can be seen from the gravity wave (GW) dispersion relation. Assuming $|\lambda_z| < 2\pi\mathcal{H}$, where $\mathcal{H}$ is the density scale height, the nonviscous GW dispersion relation is (Marks & Eckermann, 1995)

$$\omega_{Ir}^2 \simeq \frac{k_H^2 N_B^2}{m^2} + f^2, \tag{3}$$

where N_B is the buoyancy frequency, $f = 2\Omega \sin\Theta$, $\Omega = 2\pi/24$ hr is the Earth's rotation frequency, Θ is the latitude, and ω_{Ir} is the intrinsic frequency:

$$\omega_{Ir} = \omega_r - (k\bar{U} + l\bar{V}) = \omega_r - k_H U_H = k_H(c_H - U_H). \tag{4}$$

Equation (3) can be rewritten as

$$m^2 \simeq \frac{N_B^2}{(c_H - U_H)^2 - f^2/k_H^2}. \tag{5}$$

The last term in the denominator, f/k_H, is typically small for MWs, even at high latitudes where $|f|$ is maximum. For example, at 40° S, $f = -9.35 \times 10^{-5}$rad/s, which corresponds to an inertial period of $|2\pi/f| = 18.7$ hr. For a MW with $\lambda_H = 250$ km, $|f/k_H| = 4$m/s, which is typically negligible in comparison to the strong 100–150 m/s winds in the mesosphere and lower thermosphere (MLT; e.g., Larsen, 2002, Larsen et al., 2003). Since a MW has $c_H \simeq 0$, as the background wind gets quite small ($|U_H| \to |f|/k_H$), $|m| \to \infty$ in equation (5), and the MW's vertical wavelength $|\lambda_z|$ decreases rapidly to zero. This causes the MW to break just before reaching the critical level. Regardless of the mechanism which causes the MW to break, however, once a MW breaks, momentum and energy are deposited into the background flow. This process results in the excitation of smaller-amplitude secondary GWs having λ_H larger than that of the MWs (Vadas et al., 2003, 2018; Vadas & Becker, 2018).

Because the amplitudes of the diurnal and/or semidiurnal tides are large in the MLT, there are large wind reversals in this region (Larsen, 2002; Larsen et al., 2003; Figure 13 of Becker & Vadas, 2018). Thus, if a MW has survived to the mesopause region, it will not be able to propagate to the turbopause (at $z \sim 107$ km) and into the thermosphere because it will reach a critical level at some altitude within the extreme wind environment in the MLT. Thus, MWs cannot propagate into the thermosphere.

1.2. Hot Spot GWs and TADs Over the Southern Andes

The Andes Mountains is the longest continental mountain range in the world (~7,000 km), runs along the western coast of South and Central America, has an average height of ~4 km, and has widths of 200–700 km. Mount Aconcagua is the tallest mountain at nearly 7 km and is located in Argentina at 32° S and 70° W. The Andes Mountains are divided into three sections. The southern section is called the Southern Andes and is located in Argentina and Chile, south of the Llullaillaco Volcano at 24° S and 68° W.

Because the large-scale tropospheric wind system that encircles the Antarctic continent is strong, strong MW events occur over the Southern Andes. Indeed, the largest wintertime GW momentum fluxes in the southern hemisphere in the stratosphere occurs over the Southern Andes (Alexander et al., 2008; Ern et al., 2004, 2011; Jiang et al., 2003, 2006, Trinh et al., 2018; Wu, 2004; Wu et al., 2006). These "hot spot" GWs have been observed at ~30–70° S over South America by the Cryogenic Infrared Spectrometers and Telescopes for the Atmosphere at $z = 25$ km during August 1997 (Ern et al., 2004), by the High Resolution Dynamics Limb Sounder at $z = 20$–30 km during May 2006 (Alexander et al., 2008), by the Advanced Microwave Sounding Unit-A at $z = 37$ km during June–August (JJA) in 2003 (Wu, 2004; Wu et al., 2006), by the High Resolution Dynamics Limb Sounder at $z = 30$ km during July 2006 (Ern et al., 2011), by the Sounding of the Atmosphere using Broadband Emission Radiometry (SABER) at $z = 30$–70 km during July 2006 (Ern et al., 2011) and during JJ in 2010–2013 (Trinh et al., 2018), and by the Upper Atmosphere Research Satellite Microwave Limb Sounder at $z = 28$–80 km during JJA in 1992–1994 (Jiang et al., 2006). Specifically analyzing MWs with $\lambda_z > 10$ km and $\lambda_x < 100$ km, the largest MW hot spot observed by Microwave Limb Sounder at $z = 38$ km during JJA in 1992–1994 was over South America at ~35–75° S (Jiang et al., 2003). It is important to

note that these MWs weaken considerably in the mesosphere. Indeed, Trinh et al. (2018) showed that the GW hot spot in SABER (over the Southern Andes) weakened considerably at $z = 75$ km and disappeared completely at $z = 85$–90 km in JJ 2010–2013. This observation supports the model result that the MWs over the Southern Andes typically break and attenuate near the stratopause (Becker & Vadas, 2018).

Surprisingly, a wintertime "GW" hot spot over the Southern Andes is also seen in the thermosphere. Indeed, during geomagnetically quiet times, in situ wintertime data from Gravity Field and Ocean Circulation Explorer (GOCE) show a pronounced traveling atmospheric disturbance (TAD) hot spot at $z \sim 250$ km at ∼20–60° S over South America (Forbes et al., 2016; Liu et al., 2017; Trinh et al., 2018). (Here we use the term "TAD hot spot" instead of "GW hot spot" because GWs cannot be directly identified from in situ satellite measurements.) Additionally, geomagnetically quiet-time data from the Challenging Minisatellite Payload (CHAMP) show a very strong and longitudinally wide TAD hot spot at $z \sim 280$–450 km and at ∼30–70° S over South America in June during solar minimum and maximum years during 2001–2010 (Park et al., 2014; Trinh et al., 2018). These wintertime GOCE and CHAMP TAD hot spots in the thermosphere at $z \sim 250$–450 km are quite surprising because MWs cannot propagate into the thermosphere (see section 1.1).

Trinh et al. (2018) showed that the TAD hot spot over the Southern Andes in GOCE and CHAMP data correlated well with the GW activity below 75 km and that the GW hot spot weakened and disappeared in SABER at 75–90 km. With regard to the positive correlation, they wrote "Two coupling mechanisms are likely responsible for these positive correlations: (1) fast GWs generated in the troposphere and lower stratosphere can propagate directly to the T/I [thermosphere/ionosphere] and (2) primary GWs with their origins in the lower atmosphere dissipate while propagating upwards and generate secondary GWs, which then penetrate up to the T/I and maintain the spatial patterns of GW distributions in the lower atmosphere." Vadas (2007) showed that GWs launched from the troposphere typically dissipate from molecular viscosity at $z < 250$ km (pink dashed lines in left column of Figure 4 of that paper) and that such high altitudes are only attained for GWs with very large intrinsic phase speeds of $c_{IH} > 200$m/s (yellow solid lines in left column of Figure 5 of that paper), where $c_{IH} = c_H - U_H$. There is no known prolific source of GWs having such large phase speeds in the troposphere over the winter Southern Andes; therefore, it is unlikely that GWs from the troposphere could have created the GOCE and CHAMP GW hot spots. Additionally, larger-scale secondary GWs excited where MWs dissipate only have horizontal phase speeds of $c_H \sim 50$–60 m/s (Becker & Vadas, 2018; Vadas & Becker, 2018; Vadas et al., 2018). Since GWs with $c_{IH} \leq 100$m/s dissipate at or below $z \leq 175$ km (Figures 4 and 5 of Vadas, 2007), it is unlikely that secondary GWs could have created the GOCE and CHAMP TAD hot spots. What then is the source of these wintertime TAD hot spots over the Southern Andes?

In order to answer this question, it is first necessary to identify which of the hot spot TADs are GWs. We then need to determine the intrinsic parameters of the GWs (e.g., λ_H, c_{IH}, and azimuth ξ) and reverse ray trace the GWs to their possible sources. This is the investigation we undertake in this paper. A companion paper analyzes new wintertime modeling results over the Southern Andes from a high-resolution, GW-resolving global circulation model that has recently been extended into the thermosphere (Vadas & Becker, 2019). That paper finds that tertiary GWs are excited in the mesosphere and thermosphere over the Southern Andes; these tertiary GWs are generated from the local body forces created from dissipation of secondary GWs that are excited from local body forces created from MW breaking in the stratopause region.

In this paper, we perform a detailed analysis of the quiet-time hot spot TADs observed by GOCE on 5 July 2010 at 23 UT as GOCE overpassed the Southern Andes. In section 2, we create a composite map of the quiet-time GOCE TADs in JJA. In section 3, we use discrete Fourier transforms to extract the 20 largest TADs as GOCE overpassed the Southern Andes. In section 4, we search parameter space to determine which TADs are GWs using the GW dissipative polarization and dispersion relations. We then determine the intrinsic properties of the identified GWs. We ray trace these GWs to their possible sources in section 5. In section 6, we examine satellite and other data to determine whether MWs were present and if they broke over the Southern Andes earlier that day. A discussion and our conclusions are provided in sections 7 and 8, respectively.

2. GOCE Measurements and TADs

The European Space Agency GOCE mission was dedicated to precisely measure the gravity field of Earth. It was launched into a polar 0600/1800 local time (LT) Sun-synchronous orbit on 17 March 2009 and reentered on 11 November 2013. Air density and cross-track winds were derived independently from the accelerome-

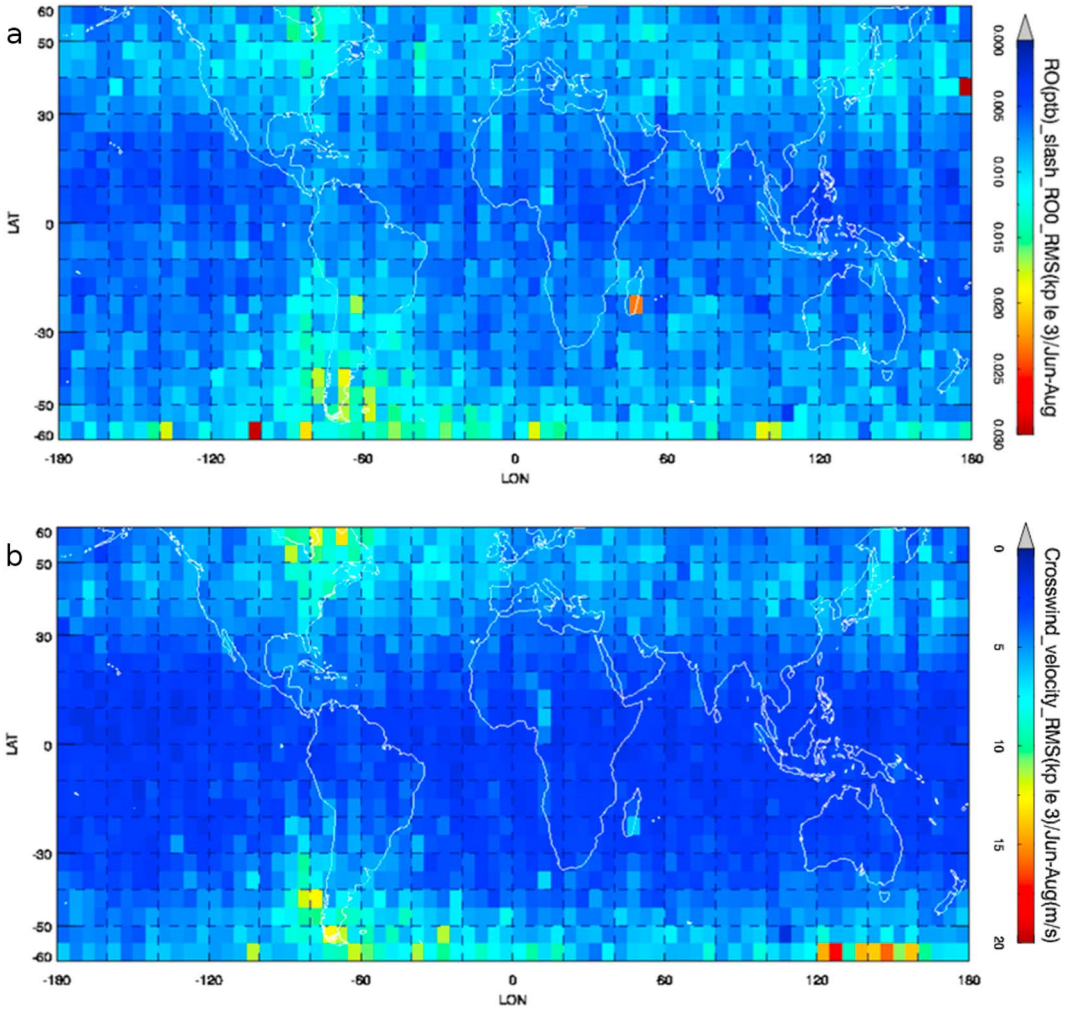

Figure 1. Traveling atmospheric perturbations from Gravity Field and Ocean Circulation Explorer having $\lambda_{\text{track}} \leq 1,000$ km when K$p < 3$ during June–August 2009–2013. (a) $\sqrt{\Sigma_i(\rho_i'/\bar{\rho}_i)^2}$. Color bar maximum is 0.03 (red). (b) $\sqrt{\Sigma_i(u'_{\text{xtrack}})^2}$. Color bar maximum is 20m/s (red). Each sum is over all "i" events in each 5° × 5° bin.

ter data and thruster accelerations via modeling radiation, satellite area, and orientation (Bruinsma, 2013; Bruinsma et al., 2014; Doornbos, 2016; Doornbos et al., 2013, 2014). The data processing involved conversion of the ion thruster activation data to accelerations, and iterative adjustment of the wind direction and air density inputs using an aerodynamic model of the satellite, until the model aerodynamic accelerations matched the observations.

Before mid-2012, GOCE's orbit was stable at $z \sim 260$–290 km. Afterward, its orbit dropped to 250 km in August 2012, to 245 km in November 2012, to 240 km in February 2013, and to 230 km in May 2013. During this time period, the LT of GOCE's orbit slowly drifted from 0600/1800 to 0730/1930 LT. Additionally, the density (wind) errors decreased on average from about 2.5% (30–40 m/s) during 2009–2010 to 1.5% (15–20 m/s) until August 2012 and then remained at ~1% (7–12 m/s) until November 2013. The useful latitude range of the GOCE data is ±60° with ~15 orbits per day, with each orbit separated by 24° longitude.

We use the V1.5 GOCE density and cross-track wind data, which is available from November 2009 to October 2013. To extract the TADs, we first calculate "background" latitudinal profiles of the density, $\bar{\rho}$, and cross-track wind, $\bar{u}_{\text{xtrack}}$, by applying a low-pass Butterworth filter to the GOCE density ρ and cross-track wind u_{xtrack}. We then calculate the density and cross-track wind perturbations, $\rho' = \rho - \bar{\rho}$ and $u'_{\text{xtrack}} = u_{\text{xtrack}} - \bar{u}_{\text{xtrack}}$, respectively, for along-track horizontal scales of the perturbations of $\lambda_{\text{track}} \leq 1,000$ km. Figure 1 shows the averaged global density and cross-track wind perturbation amplitudes in JJA 2009–2013

for both ascending and descending nodes, binned on a 5° × 5° grid. Here we only include data with Kp < 3 to minimize contamination from TADs created by large geomagnetic activity. The area that contains the largest-amplitude density perturbations in the winter hemisphere is the region over the Southern Andes. This wintertime hot spot has average density perturbations of $|\rho'|/\bar{\rho} \sim 1$–2%. This hot spot also occurs in the cross-track wind with average perturbation amplitudes of $|u'_{\text{xtrack}}| \sim 5$–15 m/s. There are also two single-bin density hot spots near Madagascar and the Antarctic Peninsula. Finally, there is a summertime hot spot in the United States over the North America Great Plains that may be due to deep convection. This hot spot coincides with the stratospheric GW hot spot from Atmospheric Infrared Sounder (AIRS) during 2003–2011 (Figures 6 and 7 of Hoffmann et al., 2013), and Hoffmann and Alexander (2010) demonstrated a high correlation between deep convection and AIRS GWs over the North America Great Plains. Note that Figure 1 is in rough agreement with previous results (Forbes et al., 2016; Liu et al., 2017; Trinh et al., 2018).

3. GW Dissipative Dispersion and Polarization Relations

Gross et al. (1984) used the phase shifts and amplitude ratios of the O and N_2 perturbations to estimate the propagation directions (to within 180°) of GWs observed by the Atmospheric Explorer-C satellite. Innis and Conde (2002) determined the GW propagation directions to within 90° from Dynamics Explorer 2 satellite measurements. Although this latter method included compressibility, it did not take into account viscous dissipation. Vadas and Nicolls (2012) generalized these approaches by including full compressibility and realistic molecular viscosity in the GW dispersion and polarization relations (originally derived by Vadas & Fritts, 2005). With this method, the phase shifts and amplitude ratios between 2 or more components of a GW (i.e., between w', u'_{xtrack}, ρ', and T') are used to determine λ_H, λ_z, ω_{Ir}, and the GW propagation direction.

We now briefly review the GW dissipative compressible dispersion and polarization relations derived by Vadas and Nicolls (2012). These relations are for medium- and high-frequency GWs, for which the Coriolis force can be neglected. At high latitudes, this occurs for GWs with periods less than 5–6 hr (Vadas et al., 2018). The zonal, meriodional, and vertical velocities of a GW are (u', v', w'), and the density and temperature perturbations are ρ' and T', respectively. Additionally, the horizontal velocity perturbation along the GW's direction of propagation is $u'_H = \sqrt{(u')^2 + (v')^2}$. We assume GW solutions of the form

$$u' = u'_0 \exp(i[kx + ly + mz - \omega_r t]), \tag{6}$$

where $\mathbf{k} = (k, l, m)$ is the wave number vector in geographic coordinates and ω_r is the observed (i.e., ground-based) frequency. We define the "hatted" GW perturbation components as

$$\hat{u} = \left[\frac{\bar{\rho}}{\bar{\rho}_0}\right]^{1/2} u', \qquad \hat{v} = \left[\frac{\bar{\rho}}{\bar{\rho}_0}\right]^{1/2} v', \qquad \hat{u}_H = \left[\frac{\bar{\rho}}{\bar{\rho}_0}\right]^{1/2} u'_H, \tag{7}$$

$$\hat{w} = \left[\frac{\bar{\rho}}{\bar{\rho}_0}\right]^{1/2} w', \qquad \hat{\rho} = \left[\frac{\bar{\rho}}{\bar{\rho}_0}\right]^{1/2} \frac{\rho'}{\bar{\rho}}, \qquad \hat{T} = \left[\frac{\bar{\rho}}{\bar{\rho}_0}\right]^{1/2} \frac{T'}{\bar{T}}, \tag{8}$$

where $\bar{T}$ and $\bar{\rho}$ are the background temperature and density, respectively, and $\bar{\rho}_0$ is the background density at a reference altitude. The compressible dissipative GW polarization relations (substituting $\widetilde{u} \to \hat{u}$, $\widetilde{v} \to \hat{v}$, $\widetilde{w} \to \hat{w}$, $\widetilde{u_H} \to \hat{u}_H$, $\tilde{T}/\bar{T} \to \hat{T}$ and $\tilde{\rho}/\rho_0 \to \hat{\rho}$ into Equations (15)–(17) and (20) of Vadas & Nicolls, 2012) are then

$$\hat{u} = \frac{k}{k_H} \hat{u}_H, \tag{9}$$

$$\hat{v} = \frac{l}{k_H} \hat{u}_H, \tag{10}$$

$$\begin{aligned} \hat{u}_H = \frac{\gamma}{i k_H c_s^2 \mathcal{D}} \Bigg[& i\omega_I \left(i\omega_I + \frac{\gamma \alpha \nu}{\text{Pr}} \right) \left(i\omega_I + \nu \left(\alpha + \frac{\text{a}}{3} (\alpha + k_H^2) \right) \right) \\ & + c_s^2 \left(m^2 + \frac{1}{4\mathcal{H}^2} \right) \left(i\omega_I + \frac{\alpha \nu}{\text{Pr}} \right) \Bigg] \hat{w}, \end{aligned} \tag{11}$$

$$\hat{T} = \frac{(\gamma - 1)}{c_s^2 \mathcal{D}} \left[\gamma i \omega_I (i\omega_I + \alpha \nu) + \frac{c_s^2}{\mathcal{H}} \left(im + \frac{1}{2\mathcal{H}} \right) \right] \hat{w}, \tag{12}$$

$$\hat{\rho} = \frac{1}{c_s^2 D}\left[\gamma\left(i\omega_I + \frac{\gamma\alpha\nu}{\mathrm{Pr}}\right)\left(i\omega_I + \nu\left(\alpha + \frac{\mathrm{a}}{3\mathcal{H}}\left(im + \frac{1}{2\mathcal{H}}\right)\right)\right) - \frac{(\gamma-1)c_s^2}{\mathcal{H}}\left(im - \frac{1}{2\mathcal{H}}\right)\right]\hat{w}. \tag{13}$$

Here

$$\mathcal{D} = \left[i\omega_I\left(\gamma im + \frac{1}{\mathcal{H}} - \frac{\gamma}{2\mathcal{H}} - \mathrm{b}\right) + \frac{\gamma\alpha\nu}{\mathrm{Pr}}\left(im + \frac{1}{2\mathcal{H}} - \mathrm{b}\right)\right], \tag{14}$$

$$\mathrm{b} = \frac{i\mathrm{a}\nu\gamma\omega_I}{3c_s^2}\left(im + \frac{1}{2\mathcal{H}}\right), \tag{15}$$

$$\alpha = -\mathbf{k}^2 + \frac{1}{4\mathcal{H}^2} + \frac{im}{\mathcal{H}}, \tag{16}$$

$$c_s^2 = \gamma g\mathcal{H} = \gamma \mathrm{r}\bar{T}, \tag{17}$$

$$N_B^2 = (\gamma-1)g^2/c_s^2, \tag{18}$$

$$\mathcal{H} = -\bar{\rho}(d\bar{\rho}/dz)^{-1} = \mathrm{r}\bar{T}/g = c_s^2/(\gamma g), \tag{19}$$

$\mathbf{k}^2 = k_H^2 + m^2$, $k_H^2 = k^2 + l^2$, N_B is the buoyancy frequency, $\tau_B = 2\pi/N_B$ is the buoyancy period, Pr is the Prandtl number, $\nu = \mu/\bar{\rho}$ is the kinematic viscosity, μ is the molecular viscosity, c_s is the sound speed, $\mathcal{H}$ is the density scale height, $\gamma = C_p/C_v$ is the ratio of specific heats, C_p and C_v are the mean specific heats at constant pressure and volume, respectively, $p = \mathrm{r}\rho T$ is the pressure, $\mathrm{r} = 8,308/\mathrm{X}_{MW}$ $\mathrm{m}^2\cdot\mathrm{s}^{-2}\cdot\mathrm{K}^{-1}$, X_{MW} is the mean molecular weight of the particle in the gas (in g/mole), and g is the gravitational constant. In addition, ω_I is the complex intrinsic frequency:

$$\omega_I = \omega_{Ir} + i\omega_{Ii}, \tag{20}$$

where ω_{Ir} is the usual intrinsic frequency and ω_{Ii} is the GW decay rate (in time). ω_I is determined via solving the compressible, complex, dissipative dispersion relation (Equation (12) of Vadas & Nicolls, 2012):

$$-\frac{\omega_I}{c_s^2}\left(\omega_I - \frac{i\gamma\alpha\nu}{\mathrm{Pr}}\right)\left(\omega_I - i\alpha\nu\right)\left(\omega_I - i\alpha\nu\left(1 + \frac{\mathrm{a}}{3}\right)\right) + \left(\omega_I - i\alpha\nu\right)\left(\omega_I - \frac{i\alpha\nu}{\mathrm{Pr}}\right)\left(\mathbf{k}^2 + \frac{1}{4\mathcal{H}^2}\right) = k_H^2 N_B^2. \tag{21}$$

Finally, $\mathrm{a} = 0$ or 1, depending on whether we include the bulk viscosity in addition to the shear viscosity in the viscous stress tensor (see Equation (1) in Vadas & Nicolls, 2012). Setting $\mathrm{a} = 0$ yields the original relations derived in Vadas and Fritts (2005). In this paper, we set $\mathrm{a} = 1$.

The zonal and meridional wave numbers determine the horizontal GW propagation direction. Namely,

$$\tan\xi = k/l, \tag{22}$$

where ξ is the azimuth angle clockwise from north. Here $k > 0$ is eastward, $k < 0$ is westward, $l > 0$ is northward, and $l < 0$ is southward.

If a GW propagates much slower than the sound speed and before it begins to dissipate from viscosity, we can substitute $c_s \to \infty$ and $\nu \sim 0$ in equation (21). We then obtain the usual anelastic GW dispersion relation for medium- and high-frequency GWs:

$$\omega_{Ir}^2 = \frac{k_H^2 N_B^2}{\mathbf{k}^2 + 1/4\mathcal{H}^2}. \tag{23}$$

Once this GW begins to dissipate in the thermosphere, however, equation (23) is no longer valid, and one must use equation (21) instead.

As an example, we choose the background atmosphere from section 4.3 at $z = 277$ km to be $\bar{T} = 727$ K, $\mathcal{H} = 35.4$ km, $\tau_B = 11.1$ min, $\gamma = 1.62$, $c_s = 752$m/s, and Pr = 0.62, with $\nu = 8.83 \times 10^5 \mathrm{m}^2/\mathrm{s}$. We set

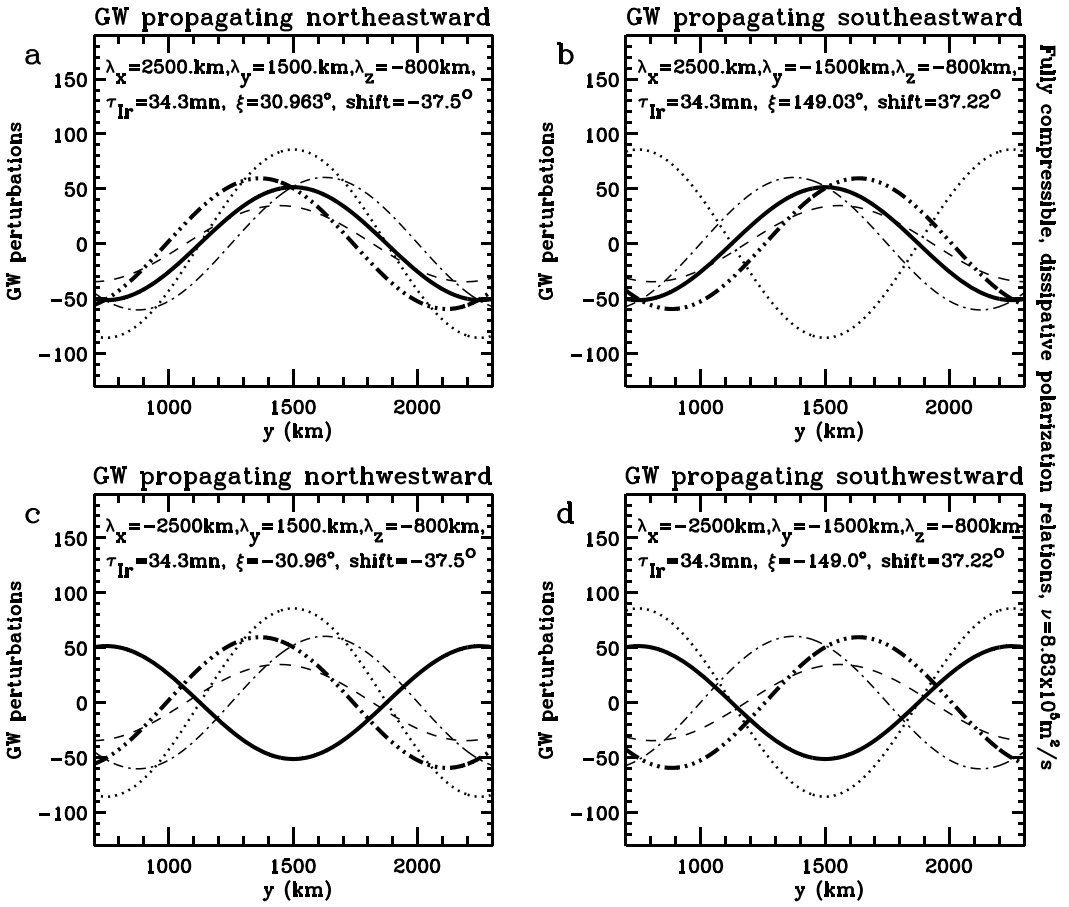

Figure 2. The behavior of large-scale example GWs. $\hat{u}$ (solid), $\hat{v}$ (dotted), $2\hat{w}$ (dash), 500 $\hat{T}$ (dash-dot), and 500 $\hat{\rho}$ (dash-dot-dot-dot) for various upward-propagating GWs having $\lambda_z = -800$ km and $\tau_{Ir} = 33.3$ min at $z = 277$ km in the thermosphere whereby $\nu = 8.83 \times 10^5 \mathrm{m}^2/s$ and Pr = 0.62. (a) Northeastward-propagating GW with $\lambda_x = 2,500$ km, $\lambda_y = 1,500$ km, and $\xi = 31.0°$. (b) Southeastward-propagating GW with $\lambda_x = 2,500$ km, $\lambda_y = -1,500$ km, and $\xi = 149.0°$. (c) Northwestward-propagating GW with $\lambda_x = -2,500$ km, $\lambda_y = 1,500$ km, and $\xi = -31.0°$. (d) Southwestward-propagating GW with $\lambda_x = -2,500$ km, $\lambda_y = -1,500$ km, and $\xi = -149.0°$. "Shift" denotes the phase shift between u'_H and ρ' along the y direction. GW = gravity wave.

$f = 0$ because the dissipative polarization relations neglect the Coriolis force (see equations (9)–(13)) and because the GOCE GWs have periods less than 1 hr (see section 4). For a given GW with wave number vector (k, l, m), we determine the real and imaginary components of its complex frequency, $\omega_I = (\omega_{Ir}, \omega_{Ii})$, via solving equation (21) iteratively using Newton's method. We then plug these values into the GW dissipative polarization relations, equations (9)–(13), to get the relationships between u', v', u'_H, w', T', and ρ'.

In Figure 2, we show snapshots (as functions of y) of the perturbation components of large-scale "example" GWs propagating northeastward, southeastward, northwestward, and southwestward at this altitude. We choose these example GWs to have $\lambda_H = 1,286$ km, $\tau_{Ir} = 33.3$ min, $\lambda_x = \pm 2,500$ km, $\lambda_y = \pm 1,500$ km, and $\lambda_z = -800$ km. Here $\lambda_x = 2\pi/k$, $\lambda_y = 2\pi/l$, and $\lambda_z = 2\pi/m$ are the zonal, meridional, and vertical wavelengths, respectively. Note that we choose large $|\lambda_z|$ compared to GWs typical in the lower and middle atmosphere because viscous dissipation removes GWs with small λ_z in the lower thermosphere (Vadas, 2007). We show the zonal velocity ($\hat{u}$), meridional velocity ($\hat{v}$), vertical velocity ($\hat{w}$), density ($\hat{\rho}$), and temperature ($\hat{T}$) perturbations from equations (9), (10), (12) and (13) in Figure 2. $\hat{u}$ and $\hat{\rho}$ are shown as thick solid and dash-dot-dot-dot lines, respectively. If the satellite track is precisely northward, then $u'_{\mathrm{xtrack}} = u'$. The absolute value of the phase shift between u'_H and ρ' for these GWs from equations (11) and (13) is 37°. Figures 2a and 2b shows that if the GW propagates northeastward (southeastward), then ρ' is maximum before (after) u'_{xtrack} is maximum along the satellite track, and the maxima of u'_{xtrack} and ρ' are phase-shifted by <90°. On the other hand, if the GW propagates northwestward (southwestward), then ρ' is maximum

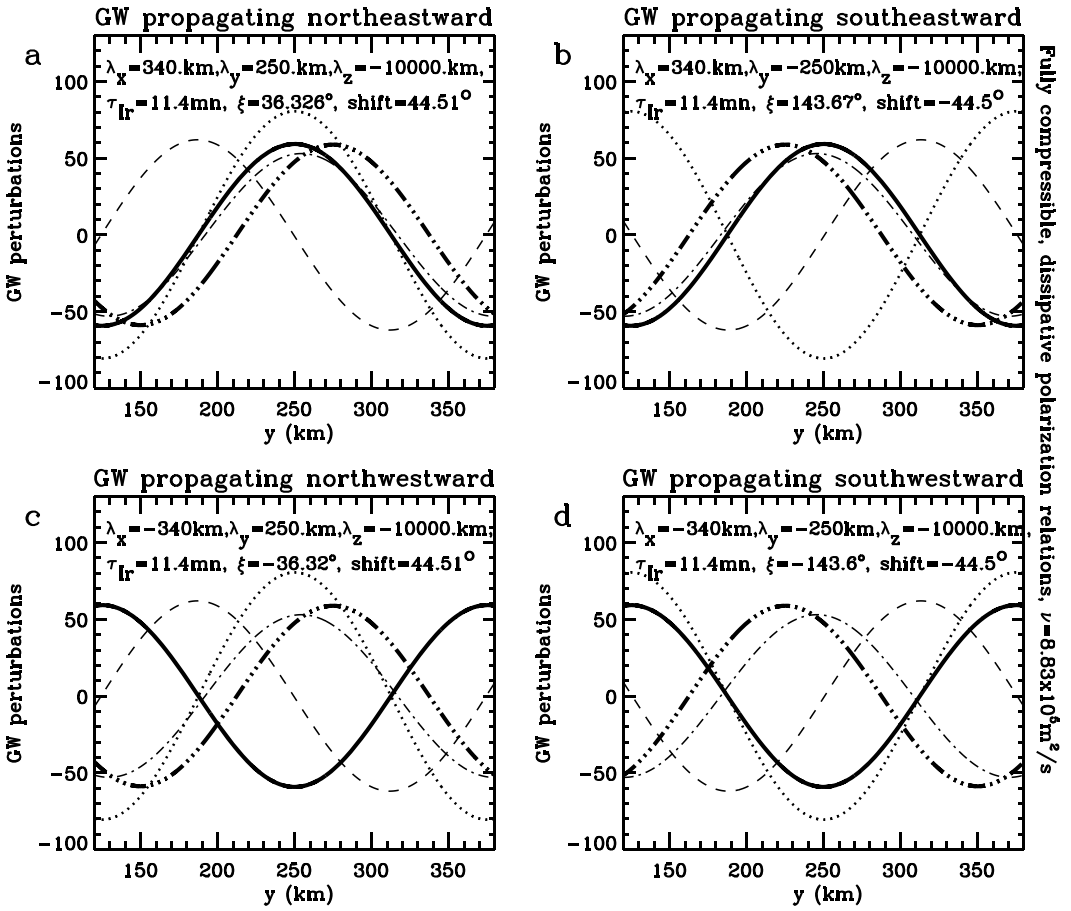

Figure 3. The behavior of medium-scale example GWs with $\omega_{Ir} \sim N_B$ and $|\lambda_z|$ very large. $\hat{u}$ (solid), $\hat{v}$ (dotted), $0.3\hat{w}$ (dash), 130 $\hat{T}$ (dash-dot), and 2,000 $\hat{\rho}$ (dash-dot-dot-dot) for various upward-propagating GWs having $\lambda_H = 201$ km, $\lambda_z = -10,000$ km, and $\tau_{Ir} = 11.4$ min at $z = 277$ km in the thermosphere whereby $\nu = 8.83 \times 10^5 m^2/s$ and Pr = 0.62. (a) Northeastward-propagating GW with $\lambda_x = 340$ km, $\lambda_y = 250$ km, and azimuth $\xi = 36.3°$. (b) Southeastward-propagating GW with $\lambda_x = 340$ km, $\lambda_y = -250$ km, and $\xi = 143.7°$. (c) Northwestward-propagating GW with $\lambda_x = -340$ km, $\lambda_y = 250$ km, and $\xi = -36.3°$. (d) Southwestward-propagating GW with $\lambda_x = -340$ km, $\lambda_y = -250$ km, and $\xi = -143.6°$. "Shift" denotes the phase shift between u'_H and ρ' along the y direction. GW = gravity wave.

before (after) u'_{xtrack} is minimum along the satellite track, and the maxima of u'_{xtrack} and ρ' are phase-shifted by 90° to 180° (see Figures 2c and 2d). In these latter cases, u'_{xtrack} flips sign relative to ρ' because the GW propagates westward.

Although it turns out that most GWs follow the phase relationship shown in Figure 2, as we will see in section 4.3, other phase relationships can occur for medium-scale GWs with extremely large vertical wavelengths and with intrinsic frequencies quite close to the buoyancy frequency: $\omega_{Ir} \sim N_B$. These GWs have $|m|$ quite close to 0 (or $|\lambda_z| \to \infty$), which occurs when an upward-propagating GW is quite close to reflecting downward (e.g., Fritts & Alexander, 2003). Such a GW can propagate deep into the thermosphere (Vadas, 2007). In Figure 3, we show snapshots of a medium-scale example GW with $\lambda_H = 201$ km, $\tau_{Ir} = 11.4$ min, $\lambda_x = \pm 340$ km, $\lambda_y = \pm 250$ km, and $\lambda_z = -10,000$ km. The absolute value of the phase shift between u'_H and ρ' from equations (11) and (13) is 44.5°. Because $|\lambda_z|$ is so large, this GW is close to reflecting downward because $|m| \sim 0$ and $\tau_{Ir} \sim \tau_B$. In a $z - t$ plot measured by a ground-based observer, this GW's phase lines would be close to vertical at this altitude. GWs having nearly vertical phase lines and extremely large $|\lambda_z|$ were observed over Poker Flat, Alaska, during the winter; however, because of changes in the background wind and temperature with altitude, this phenomenon occurred over shallow vertical depths of only 10–30 km (see Figures 2 and 8 of Vadas & Nicolls, 2009). Therefore, we can still apply our theory here (i.e., assume that c_s, $\mathcal{H}$, etc, are constant in z) as long as the vertical depth of the region where the GW's phase slopes are nearly vertical is not too large.

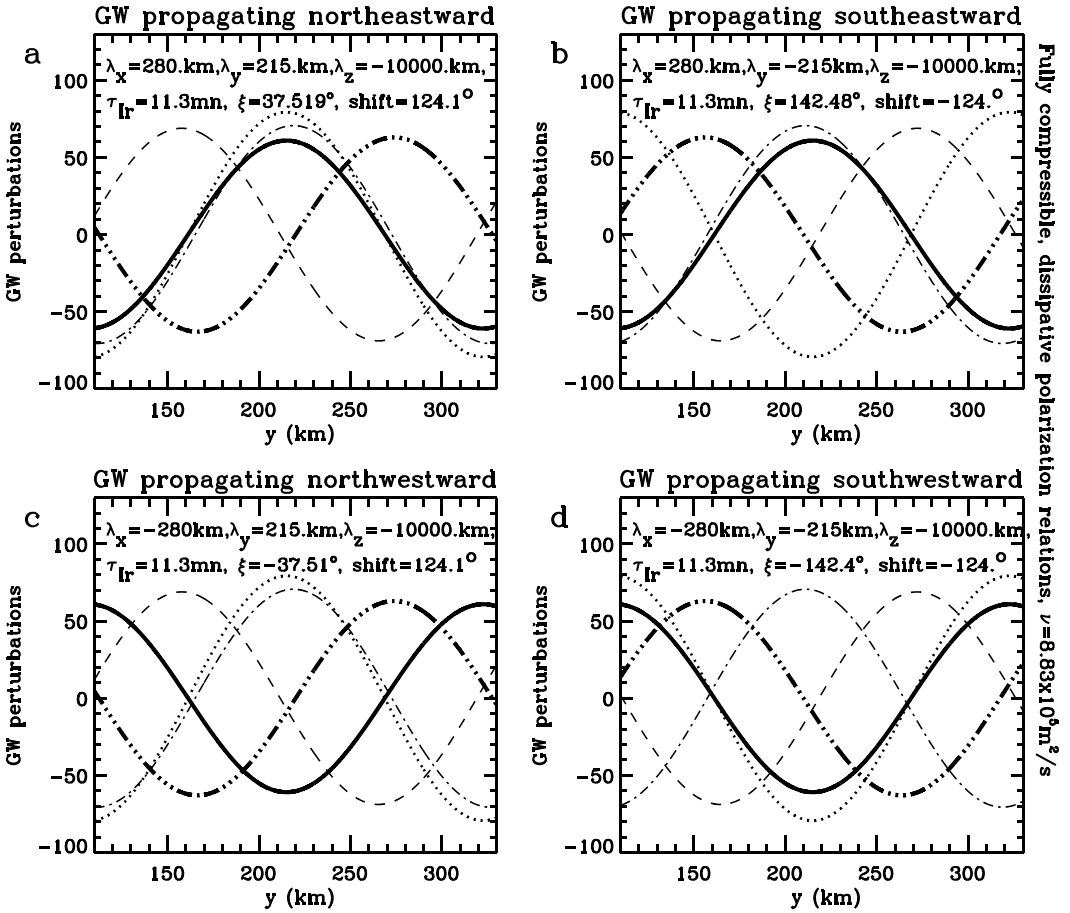

Figure 4. The behavior of medium-scale example GWs with $\omega_{Ir} \sim N_B$ and $|\lambda_z|$ very large. $\hat{u}$ (solid), $\hat{v}$ (dotted), $0.3\hat{w}$ (dash), 140 $\hat{T}$ (dash-dot), and 1,000 $\hat{\rho}$ (dash-dot-dot-dot) for various upward-propagating GWs having $\lambda_H = 170.5$ km, $\lambda_z = -10,000$ km, and $\tau_{Ir} = 11.3$ min at $z = 277$ km in the thermosphere whereby $\nu = 8.83 \times 10^5$ m^2/s and Pr = 0.62. (a) Northeastward-propagating GW with $\lambda_x = 280$ km, $\lambda_y = 215$ km, and azimuth $\xi = 37.5°$. (b) Southeastward-propagating GW with $\lambda_x = 280$ km, $\lambda_y = -215$ km, and $\xi = 142.5°$. (c) Northwestward-propagating GW with $\lambda_x = -280$ km, $\lambda_y = 215$ km, and $\xi = -37.5°$. (d) Southwestward-propagating GW with $\lambda_x = -280$ km, $\lambda_y = -215$ km, and $\xi = -142.5°$. "Shift" denotes the phase shift between u'_H and ρ' along the y direction. GW = gravity wave.

Figures 3a and 3b show that if this medium-scale, high-frequency example GW propagates southeastward (northeastward), then ρ' is maximum before (after) u'_{xtrack} is maximum along the track, and the maxima of u'_{xtrack} and ρ' are phase-shifted by <90°. On the other hand, if the GW propagates southwestward (northwestward), then ρ' is maximum before (after) u'_{xtrack} is minimum along the track, and the maxima of u'_{xtrack} and ρ' are phase-shifted by 90° to 180° (see Figures 3c and 3d).

In Figure 4, we show snapshots of a somewhat smaller medium-scale example GW with $\lambda_H = 170.5$ km, $\tau_{Ir} = 11.3$ min, $\lambda_x = \pm 280$ km, $\lambda_y = \pm 215$ km, and $\lambda_z = -10,000$ km. The absolute value of the phase shift between u'_H and ρ' from equations (11) and (13) is 124°. Figures 4c and 4d show that if this medium-scale, high-frequency example GW propagates northwestward (southwestward), then ρ' is maximum before (after) u'_{xtrack} is maximum along the track, and the maxima of u'_{xtrack} and ρ' are phase-shifted by <90°. On the other hand, if the GW propagates northeastward (southeastward), then ρ' is maximum before (after) u'_{xtrack} is minimum along the track, and the maxima of u'_{xtrack} and ρ' are phase-shifted by 90° to 180° (see Figures 4a and 4b). Note that the phase relationships are different in Figures 2-4 and are due to the differences in the

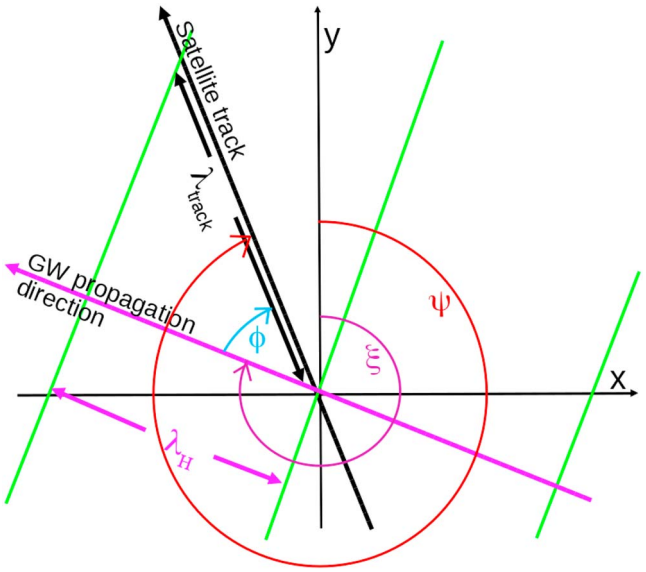

Figure 5. Satellite track (black arrow), GW propagation direction (pink arrow), and GW lines of constant phase (green parallel lines). λ_{track} is the distance between GW maxima along the satellite track, and λ_H is the GW horizontal wavelength. ϕ is the angle between the satellite track and the GW propagation direction. ψ is the azimuth (east of north) of the satellite track (red). ξ is the GW's azimuth (pink). GW = gravity wave.

phase shift between u'_H and ρ'. This will become clearer when we display the phase relationships for a broad range of GWs in section 4.3.

4. GOCE Hot Spot TADs and Identified GWs Over the Southern Andes on 5 July 2010

4.1. Layout of a GW Observed In Situ by a Satellite

Figure 5 shows a sketch of a satellite moving at an azimuth ψ (clockwise from north). Because this satellite is moving northwestward, ψ is negative. It also shows a northwestward-propagating GW having an azimuth ξ and horizontal wavelength λ_H. The distance between the maxima of the GW perturbations along the satellite track is λ_{track}. Because the satellite does not align in general with the GW propagation direction, $\lambda_{track} \geq \lambda_H$. We define the angle between the satellite path and the GW propagation direction to be ϕ, where

$$\phi = \psi - \xi. \tag{24}$$

Since

$$\lambda_H = \lambda_{track} |\cos \phi|, \tag{25}$$

if ϕ can be determined and λ_{track} is measured, we can then calculate λ_H from equation (25).

4.2. Extraction of TADs From GOCE Density and Cross-Track Wind

On 5 July 2010 at 23 UT during orbit 13, GOCE was traveling northwestward over South America, as shown in Figure 6a. Because Kp < 3, geomagnetic activity was not significant at this time. Figure 6b shows GOCE's path as a function of longitude and latitude along the chosen track length (solid line); this is the track length we analyze below. GOCE's azimuth was $\psi = -11.365°$ at this time. The distance along this track length from 53° to 20° S is also shown as a function of latitude in Figure 6b (solid line and upper x axis). The total distance along this track length is

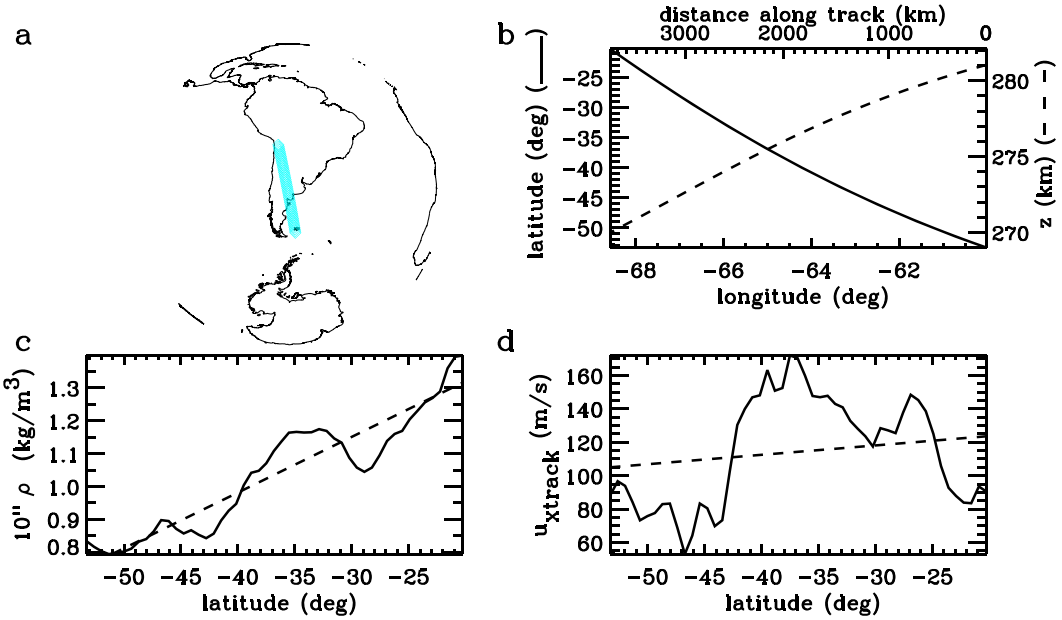

Figure 6. (a) GOCE ascending path of orbit 13 at 23:04–23:12 UT on 5 July 2010 (blue). (b) GOCE's path as a function of longitude and latitude (solid line). The distance along the track from 53° S (solid line and upper x axis). GOCE's path as a function of longitude and altitude (dashed line and right-hand y axis). (c) $10^{11}\rho$ (solid line) and the linear fit, $10^{11}\bar{\rho}$ (dashed line). (d) Cross-track wind, u_{xtrack} (solid line), and the linear fit, $\bar{u}_{xtrack}$ (dashed line). GOCE = Gravity Field and Ocean Circulation Explorer.

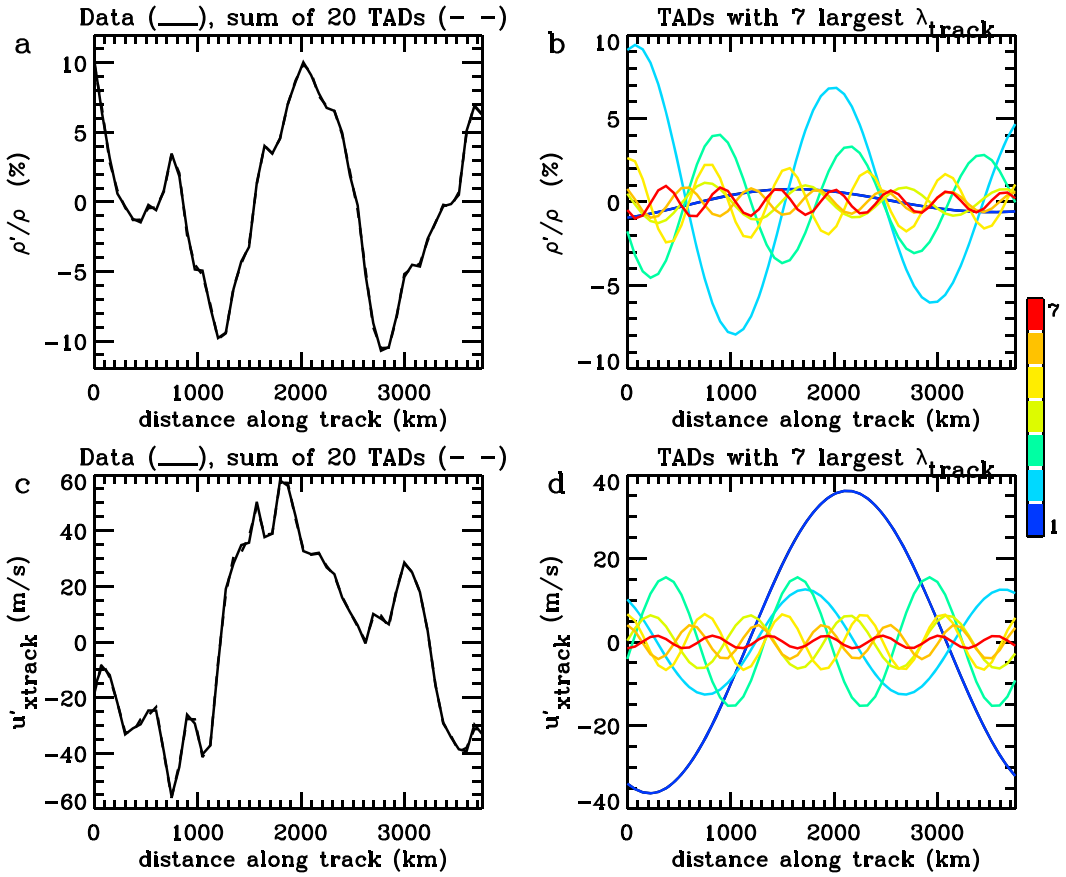

Figure 7. (a) The density perturbation, $\rho'/\bar{\rho} = (\rho - \bar{\rho})/\bar{\rho}$ (solid), where $\bar{\rho}$ is the linear fit of ρ (i.e., dashed line in Figure 6c). The sum of the density perturbations, $\rho'/\bar{\rho}$, for the TADs with the 20 largest values of λ_{track} (dashed). (b) $\rho'/\bar{\rho}$ for the TADs with the seven largest values of λ_{track} (color from blue to red shows the TAD #). (c) The cross-track wind perturbation, $u'_{\text{xtrack}} = u_{\text{xtrack}} - \bar{u}_{\text{xtrack}}$ (solid), where $\bar{u}_{\text{xtrack}}$ is the linear fit of u_{xtrack} (i.e., dashed line in Figure 6d). The sum of u'_{xtrack} for the TADs with the 20 largest values of λ_{track} (dashed). (d) u'_{xtrack} for the TADs with the 7 largest values of λ_{track} (color shows the TAD #). TAD = traveling atmospheric disturbance.

3,822 km. The average distance between data points is ~75 km. We also show the satellite altitude as a function of longitude (dashed line and right-hand y axis). We see that GOCE's altitude decreased from $z \sim 280$ to 270 km along the track length. Figure 6c shows the total density (ρ) and the linear fit to ρ (which is defined as the background density $\bar{\rho}$) as functions of latitude. The increase of $\bar{\rho}$ occurs because of the decrease of the satellite's altitude along the track length (see Figure 6b). Figure 6d shows the total cross-track wind (u_{xtrack}) and the linear fit to u_{xtrack} (defined as the background cross-track wind $\bar{u}_{\text{xtrack}}$, which mainly reflects the zonal background wind here) as functions of latitude. $\bar{u}_{\text{xtrack}}$ is positive (i.e., is mainly eastward), with an average amplitude of ~110 m/s. (Note that the mean GOCE cross-track winds are known to be somewhat too large in the northern hemisphere [Dhadly et al., 2017], although the applicability of this result to the southern hemisphere is unknown.)

We now extract the TADs from this data. The solid lines in Figures 7a and 7c show $\rho'/\bar{\rho} = (\rho - \bar{\rho})/\bar{\rho}$ and $u'_{\text{xtrack}} = u_{\text{xtrack}} - \bar{u}_{\text{xtrack}}$, respectively. Here $\bar{\rho}$ and $\bar{u}_{\text{xtrack}}$ are the linear fits to ρ and u_{xtrack}, respectively, along the track length. We extract the TADs from ρ' and u'_{xtrack} separately by applying a discrete Fast Fourier Transform with respect to the distance along the chosen track length to each, assuming $\lambda_{\text{track}} = 3,822$ km for the first Fourier mode. The sum of $\rho'/\bar{\rho}$ and u'_{xtrack} for the resulting TADs having the 20 largest values of λ_{track} (i.e., the first 20 Fourier modes) is shown in Figures 7a and 7c, respectively, as dashed lines. It is difficult to see the dashed lines because they overlay the solid lines nearly exactly. Because of this, we conclude that these 20 TADs contain nearly all of the variability in $\rho'/\bar{\rho}$ and u'_{xtrack}. (Note that the twentieth Fourier mode has $\lambda_{\text{track}} \sim 190$ km, which is close to the smallest TAD extractable from the data set, since the distance between

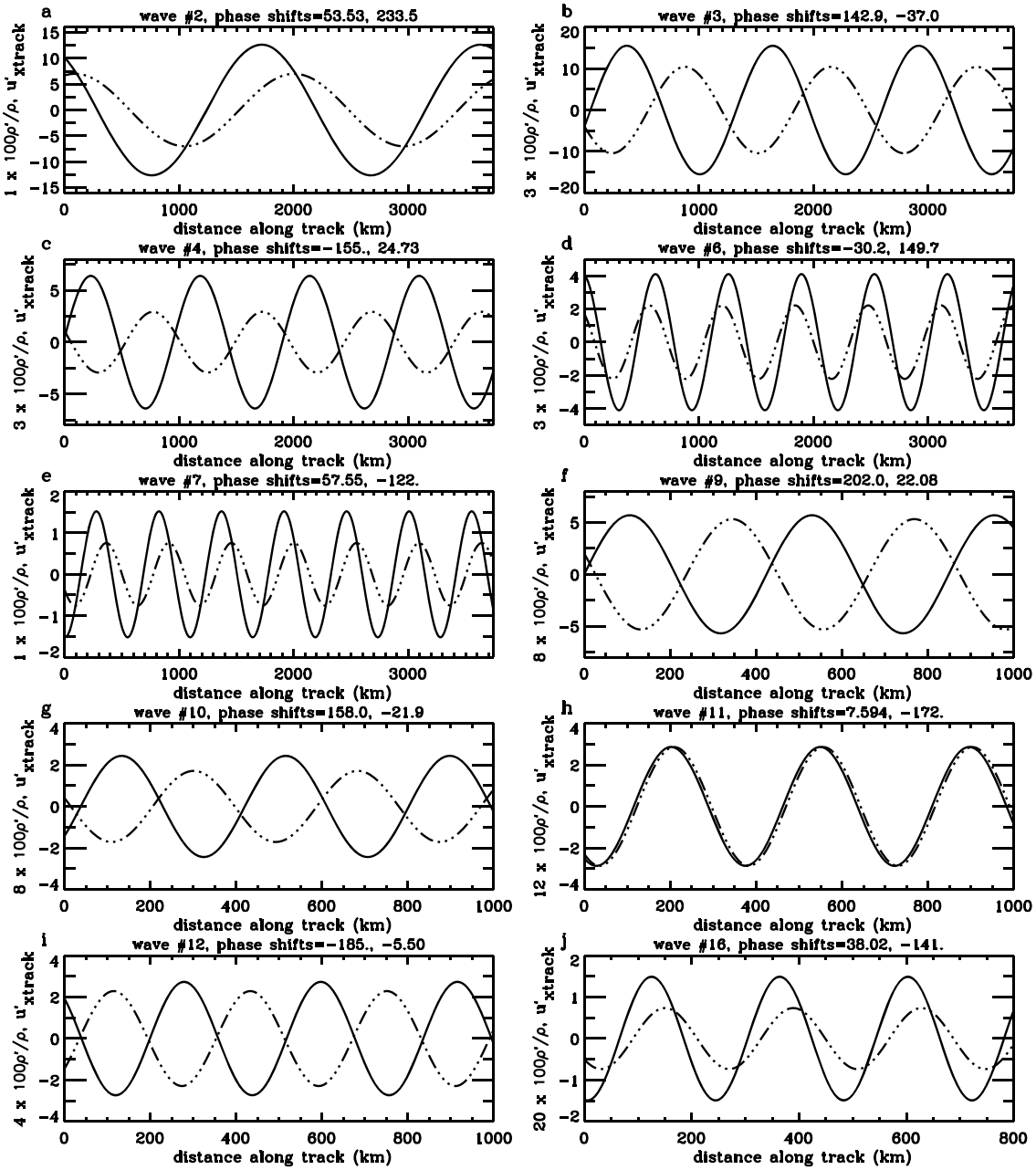

Figure 8. (a–j) $\beta \times 100\rho'/\bar{\rho}_{avg}$ (dash-dot-dot-dot) and u'_{xtrack} (solid, in m/s) for traveling atmospheric disturbances 2–4, 6, 7, 9–12, and 16, respectively. Here $100\rho'/\bar{\rho}_{avg}$ is multiplied by the integer β to see the phase difference between ρ' and u'_{xtrack} more clearly, and $\bar{\rho}_{avg}$ is the average value of $\bar{\rho}$. The value of β is labeled on the y axis of each panel. The title of each panel lists the phase shifts between ρ' and u'_{xtrack} and between ρ' and $-u'_{\text{xtrack}}$, respectively, in degrees.

data points is ~75 km.) Figures 7b and 7d show the TADs having the seven largest values of λ_{track} (i.e., the first seven Fourier modes) for $\rho'/\bar{\rho}$ and u'_{xtrack}, respectively.

Figure 8 shows $\rho'/\bar{\rho}_{avg}$ and u'_{xtrack} for 10 of the TADs. Here, $\bar{\rho}_{avg}$ is the average value of $\bar{\rho}$. These TADs have $\lambda_{\text{track}} \sim$ 230–1,900 km, and have various phase and amplitude relationships between ρ' and u'_{xtrack}. In the title of each panel, we include the phase shifts between ρ' and u'_{xtrack} and between ρ' and $-u'_{\text{xtrack}}$ in degrees. Positive (negative) phase shifts correspond to u'_{xtrack} peaking before (after) ρ' along the satellite path. This phase shift is important for determining a GW's propagation direction. For example, because the phase difference between ρ' and u'_{xtrack} is 53.53° for TAD 2 in Figure 8a, if this TAD was a GW, then it must have propagated (1) southeastward relative to the satellite track if it had normal values of $|\lambda_z|$ and ω_{Ir} (see

Table 1
Parameters of the Traveling Atmospheric Disturbances (TADs) From Gravity Field and Ocean Circulation Explorer Data, $\psi = -11.365°$

TAD	λ_{track} (km)	|Phase shift|	$\rho'/\bar{\rho}_{avg}$ (%)	u'_{xtrack} (m/s)	$\frac{100\rho'/\bar{\rho}_{avg}}{u'_{\text{xtrack}}}$ (s/m)	Phase shifts
1	3,821.7	44.0 ± 1.6	0.750 ± 0.024	36.25 ± 1.81	0.021 ± 0.002	−43.9, −223.
2	1,910.7	53.5 ± 1.2	6.992 ± 0.122	12.62 ± 0.67	0.554 ± 0.040	53.53, 233.5
3	1,273.8	37.0 ± 0.9	3.475 ± 0.056	15.51 ± 0.58	0.224 ± 0.012	142.9, −37.0
4	955.3	24.7 ± 1.9	0.977 ± 0.019	6.40 ± 0.50	0.153 ± 0.015	−155., 24.73
5	764.4	17.1 ± 1.2	1.965 ± 0.034	6.69 ± 0.32	0.294 ± 0.019	17.11, 197.1
6	636.9	30.2 ± 1.5	0.739 ± 0.015	4.11 ± 0.25	0.180 ± 0.015	−30.2, 149.7
7	546.0	57.6 ± 3.1	0.755 ± 0.015	1.52 ± 0.21	0.497 ± 0.081	57.55, −122.
8	477.7	78.0 ± 1.5	0.216 ± 0.005	2.85 ± 0.17	0.076 ± 0.006	102.0, −77.9
9	424.6	22.1 ± 0.5	0.666 ± 0.011	5.70 ± 0.09	0.117 ± 0.004	202.0, 22.08
10	382.1	22.0 ± 0.8	0.214 ± 0.004	2.44 ± 0.07	0.088 ± 0.004	158.0, −21.9
11	347.4	7.6 ± 0.8	0.239 ± 0.005	2.87 ± 0.08	0.083 ± 0.004	7.594, −172.
12	318.5	5.5 ± 0.6	0.573 ± 0.009	2.74 ± 0.06	0.209 ± 0.008	−185., −5.50
13	294.0	63.1 ± 0.5	0.319 ± 0.006	3.46 ± 0.05	0.092 ± 0.003	−243., −63.1
14	273.0	45.7 ± 3.4	0.299 ± 0.005	0.60 ± 0.10	0.498 ± 0.089	134.3, −45.6
15	254.8	88.9 ± 1.9	0.359 ± 0.006	0.82 ± 0.07	0.440 ± 0.045	−88.8, 91.13
16	238.8	38.0 ± 1.5	0.037 ± 0.001	1.49 ± 0.08	0.025 ± 0.002	38.02, −141.
17	224.8	41.9 ± 1.5	0.280 ± 0.005	1.32 ± 0.09	0.212 ± 0.018	41.86, 221.8
18	212.3	13.2 ± 5.3	0.076 ± 0.001	0.33 ± 0.08	0.228 ± 0.061	−13.2, 526.7
19	201.2	12.3 ± 3.4	0.188 ± 0.003	0.50 ± 0.08	0.375 ± 0.064	−12.2, 167.7
20	191.1	18.9 ± 0.8	0.052 ± 0.001	1.43 ± 0.04	0.036 ± 0.002	198.9, 18.94

Figure 2b) or (2) northeastward relative to the satellite track if it was a medium-scale GW with an extremely large value of $|\lambda_z|$ and $\omega_{Ir} \sim N_B$ (see Figure 3a). Note that because $|u'_H|$ and $|u'_{\text{xtrack}}|$ peak at the same locations along the satellite track (see Figures 2-4), the absolute value of the phase difference between $|u'_H|$ and $|\rho'|$ is the same as the absolute value of the phase difference between $|u'_{\text{xtrack}}|$ and $|\rho'|$.

We list the TADs having the 20 largest values of λ_{track} in Table 1. From left to right is the TAD #, λ_{track}, the absolute value of the minimum phase shift between $|\rho'|$ and $|u'_{\text{xtrack}}|$ in degrees, the amplitude of $100\rho'/\bar{\rho}_{avg}$, the amplitude of u'_{xtrack}, the amplitude of $(100\rho'/\bar{\rho}_{avg})$ divided by the amplitude of u'_{xtrack}, and the phase shifts between ρ', u'_{xtrack}, and $-u'_{\text{xtrack}}$ in degrees. In the last column, the first phase shift is between ρ' and u'_{xtrack}, while the second phase shift is between ρ' and $-u'_{\text{xtrack}}$. As before, a positive (negative) phase shift corresponds to u'_{xtrack} peaking before (after) ρ' along the satellite path. Note that λ_{track} ranges from ∼ 190 to 3,850 km.

4.3. Determining Which TADs Are GWs and Determining the Intrinsic Parameters of the Identified GWs

In this section, we use GW dissipative theory to determine (1) which GOCE TADs are GWs and (2) what the intrinsic properties of the identified GWs are. This method requires the values of $\mathcal{H}$, X_{MW}, N_B, c_s, ν, Pr, and γ at the observation time. On 5 July 2010 at 23 UT, GOCE was located at 40°S and 64°W at the altitude of $z = 277$ km. To estimate $\mathcal{H}$, X_{MW}, N_B, and so forth, we utilize the empirical NRLMSISE-00 model (Hedin, 1991). Figure 9 shows this background atmosphere, along with the background zonal and meridional winds from the Horizontal Wind Model 14 (Drob et al., 2015).

At $z = 277$ km and 40° S, we obtain $\bar{T} = 727$ K, $\bar{\rho} = 1.28 \times 10^{-8}$ g/m^3, $\mathcal{H} = 35.4$ km, $N_B = 9.40 \times 10^{-3}$rad/s, $\tau_B = 11.1$ min, $\gamma = 1.62$, $X_{\text{MW}} = 17.3$ g/mol, $c_s = 752$m/s, and $f = 0$. We set Pr = 0.62 because this value most closely reflects the thermal diffusivity in the thermosphere for $z < 500$ km (Vadas & Crowley, 2017). Note that the NRLMSISE-00 value for $\bar{\rho}$ agrees reasonably well with GOCE's observed value of $\bar{\rho} = 9.68 \times 10^{-9}$ g/m^3. Additionally, the background wind from the Horizontal Wind Model 14 is mostly eastward with $\bar{U} = 141$ m/s and $\bar{V} = -22$ m/s, which agrees reasonably well with the approximate eastward direction of $\bar{u}_{\text{xtrack}}$ measured by GOCE (see Figure 6d).

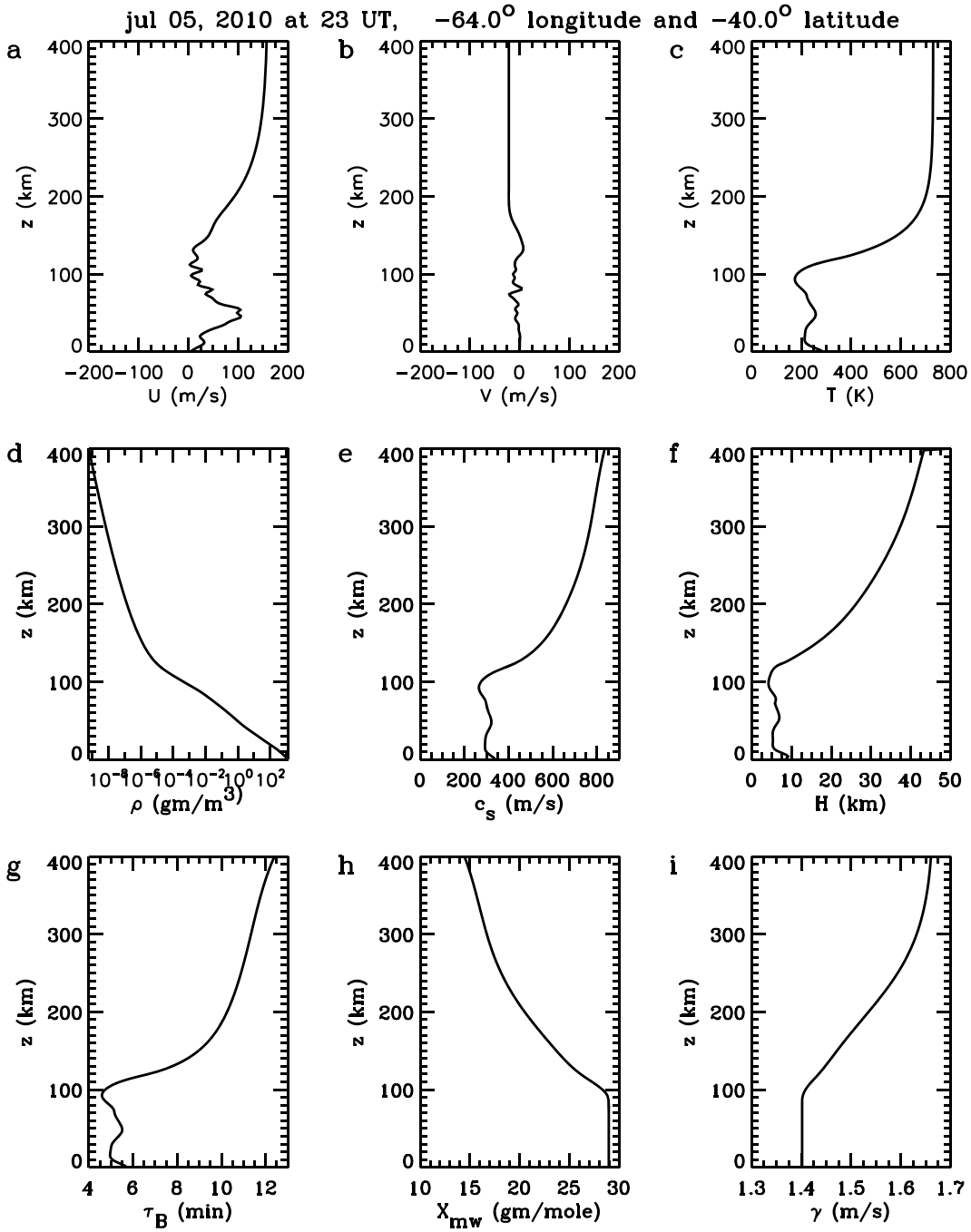

Figure 9. The background atmosphere used for ray tracing on 5 July 2010 at 23 UT at 64° W and 40° S. $\bar{U}$ (a), $\bar{V}$ (b), $\bar{T}$ (c), $\bar{\rho}$ (d), c_s (e), $\mathcal{H}$ (f), τ_B (g), X_{MW} (h), and γ (i).

The standard formula for the molecular viscosity is

$$\mu = \frac{\left(4.03 n_{O_2} + 3.43 n_{N_2} + 3.90 n_O + 3.84 n_{He} + 1.22 n_H\right) \times 10^{-4}\, \bar{T}^{0.69}}{n_{O_2} + n_{N_2} + n_O + n_{He} + n_H} \mathrm{gm}^{-1}\,\mathrm{s}^{-1}, \tag{26}$$

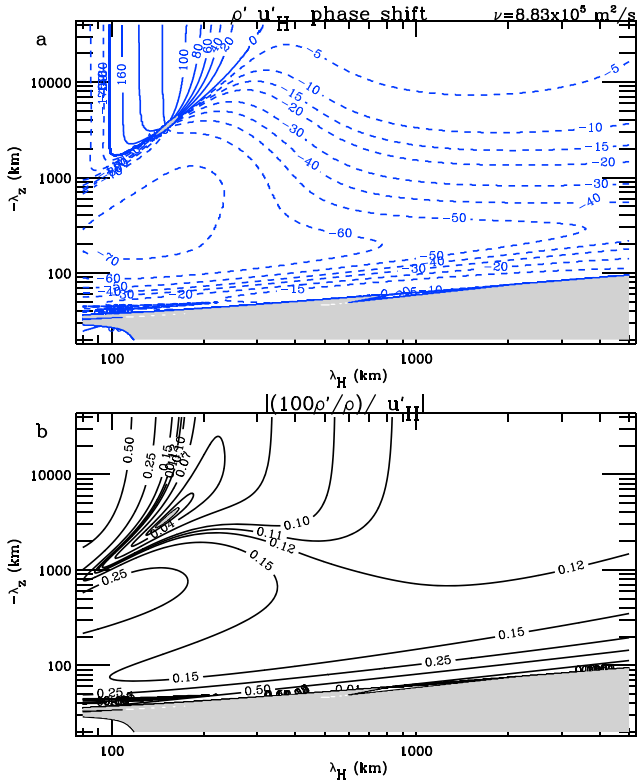

Figure 10. (a) The phase shift between ρ' and u'_H for GWs along their propagation direction (blue lines, in degrees). Solid (dash) lines denote positive (negative) values. (b) The amplitude ratio $(100\rho'/\bar{\rho})/u'_H$ for the GWs from (a) (black lines, in s/m). The gray shaded regions are for GWs with $\left|\frac{100\rho'/\bar{\rho}}{u'_H}\right| < 0.01$ s/m. GW = gravity wave.

where n_i is the number of molecules per cubic meter of the ith species (Equations (14.34)–(14.40) in Banks & Kockarts, 1973). For $z < 450$ km, equation (26) is nearly identical to the simpler expression

$$\bar{u}_{\text{xtrack}} \tag{27}$$

(Vadas & Crowley, 2017). Using the above values of $\bar{T}$ and $\bar{\rho}$ from MSIS, equation (27) yields $\nu = 2.81 \times 10^6$ m^2/s.

Vadas and Crowley (2017) found that if equations (26) or (27) are used for μ, then a serious discrepancy results between GW dissipative theory and several data sets. They found that this discrepancy arises because μ is too large for $z \geq 220$ km and argued that this likely occurs because the mean free path is a significant fraction of the density scale height at $z \sim 220$ km. They explored several different functional forms for μ and found reasonably good agreement between GW theory and data if μ is given by

$$\mu = \begin{cases} 3.34 \times 10^{-4} \bar{T}^{0.71} \ \text{gm}^{-1}\text{s}^{-1} & \text{for} \quad z < z_\mu \\ \mu(z_\mu)\left(\frac{\bar{\rho}}{\bar{\rho}(z_\mu)}\right)^{\beta/3} & \text{for} \quad z \geq z_\mu, \end{cases} \tag{28}$$

where $z_\mu = 220$ km and $\beta = 2$. Here $\mu(z_\mu)$ and $\bar{\rho}(z_\mu)$ are the values of μ and $\bar{\rho}$ at $z = z_\mu$, respectively. This functional form for μ results in $|\lambda_z|$ increasing less rapidly with altitude at $z > 220$ km than predicted theoretically by Vadas (2007); this has been observed at the Arecibo Observatory (Figure 13a of Nicolls et al., 2014). We utilize equation (28) here, because it likely better represents the molecular viscosity in the thermosphere. At GOCE's time and location, equation (28) yields $\nu = 8.83 \times 10^5$m^2/s. This is the value we use here.

We now combine equations (11) and (13) to obtain the complex polarization relation between ρ' and u'_H for GWs propagating in a background atmosphere defined by the parameters given in the first paragraph of section 4.3. (Note that this is the same background atmosphere as used in Figures 2-4.) Figures 10a and 10b show the phase shifts and amplitude ratios, respectively, between ρ' and u'_H for GWs having $\lambda_H = 80$ to 5,000 km and $|\lambda_z| = 20$ to 40,000 km. The phase shift is defined as $[x_H(\max(\rho)) - x_H(\max(u_H))]/\lambda_H$, where $x_H(\max(\rho))$ and $x_H(\max(u_H))$ are the locations along the GW propagation direction where ρ and u_H are maximum, respectively. Positive (negative) phase shifts correspond to u'_H lagging (leading) ρ' along the x_H direction. This shift is negative for all large-scale and most medium-scale GWs, such that u'_H leads ρ'. Since $|u'_{\text{xtrack}}| \leq |u'_H|$,

$$\left|\frac{100\rho'/\bar{\rho}}{u'_{\text{xtrack}}}\right| \geq \left|\frac{100\rho'/\bar{\rho}}{u'_H}\right|. \tag{29}$$

Since $\left|\frac{100\rho'/\bar{\rho}_{avg}}{u'_{\text{xtrack}}}\right| \geq 0.01$ s/m for all TADs in Table 1, we only include GWs with $\left|\frac{100\rho'/\bar{\rho}}{u'_H}\right| \geq 0.01$ s/m in Figure 10. Given an exact phase shift and amplitude ratio between ρ' and u'_H, it is clear that λ_H, λ_z, ω_{Ir}, and the propagation direction can be determined uniquely from Figure 10. For all medium- and large-scale GWs with $\lambda_H > 300$ km and for all medium-scale GWs with $\lambda_H < 300$ km and $|\lambda_z| \leq 1,000$ km (dashed lines in Figure 10a), the propagation directions are given by the qualitative results of Figure 2. That is, (1) if ρ' peaks before (after) u'_{xtrack} along the track, and they peak within 90° of each other, then the GW propagates northeastward (southeastward), or (2) if ρ' peaks before (after) $-u'_{\text{xtrack}}$ along the track, and they peak within 90° of each other, then the GW propagates northwestward (southwestward). For high-frequency, medium-scale GWs with very large $|\lambda_z|$ and $\omega_{Ir} \sim N_B$, the propagation directions are given by the qualitative results of Figures 3 and 4. Note that because of the "discontinuity" in the phase shift at $\lambda_H \sim 100$–300 km and $|\lambda_z| \sim$ 1,000–10,000 km (see Figure 10a), the propagation direction may not be uniquely determined after error bars have been included for these GWs.

If a GW propagates perpendicular to the satellite track (i.e., approximately zonally for a northward-moving satellite), then $u'_{\text{xtrack}} \simeq u'_H$ and

$$\left|\frac{100\rho'/\bar{\rho}}{u'_{\text{xtrack}}}\right| \simeq \left|\frac{100\rho'/\bar{\rho}}{u'_H}\right|. \tag{30}$$

However, if a GW propagates parallel to the satellite track (i.e., approximately meridionally for a northward-moving satellite), then $u'_{\text{xtrack}} \ll u'_H$, so that

$$\left|\frac{100\rho'/\bar{\rho}}{u'_{\text{xtrack}}}\right| \gg \left|\frac{100\rho'/\bar{\rho}}{u'_H}\right|. \tag{31}$$

For most medium-scale and all large-scale GWs, $|(100\rho'/\bar{\rho})|/|u'_H| \sim 0.1$–$0.25$ (see Figure 10b). Combining this with equation (31) and Table 1, we infer that if TADs 2, 7, 14, 15, and 19 were GWs, then they likely propagated mainly meridionally. We see below that this is true for all TADs except 15, which is not identified as a GW.

We now assume that the phase shifts and amplitude ratios between ρ' and u'_H in Figure 10 are correct for all of the GWs observed by GOCE over the chosen track length. Figure 11 shows the results of a rough analysis used to determine if TADs 2, 4, and 7 were GWs, and if so, what their intrinsic parameters were. For each TAD, we know λ_{track} and the phase shift and amplitude ratios between ρ' and u'_{xtrack} (see Table 1). Using Figure 5, ϕ is related to the measured amplitude ratio via

$$\sin\phi = \frac{u'_{\text{xtrack,meas}}}{u'_{H,0}} = \left\{\frac{u'_{\text{xtrack,meas}}}{(100\rho'_{\text{meas}}/\bar{\rho}_{avg})}\right\} \quad \left[\frac{(100\rho'_0/\bar{\rho})}{u'_{H,0}}\right], \tag{32}$$

where the subscript "0" refers to the GW amplitude, and the subscript "meas" refers to the measured values. We perform two nested do loops which range over all theoretical GWs having $\lambda_H = 80$ to 5,000 km and $|\lambda_z| = 20$ to 40,000 km in Figure 10. For each theoretical GW, we calculate what ϕ would be from equation (32) if the GW had the same amplitude ratio as that of the TAD (column 6 of Table 1). (Here the ratio in square brackets in equation (32) is computed from the GW dissipative polarization relations (i.e., the values are taken directly from Figure 10b), and the ratio in curly brackets is taken from column 6 of Table 1. Note that we do not include the error bars on this ratio for this rough estimate; these errors are included below using a more complete analysis method.) We then use equation (25) to calculate what λ_{track} would be for each theoretical GW if it had this assumed amplitude ratio.

Figure 11a shows the resulting calculated values of λ_{track} (long dashed dark green lines) for the theoretical GWs having the assumed amplitude ratio for TAD 2. We also overplot the phase difference between ρ' and u'_H for these theoretical GWs (dashed blue lines). These dashed blue lines are the same as the dashed blue lines in Figure 10a. At this point, only the measured amplitude ratio for TAD 2 has been used to constrain the parameters of the theoretical GWs. We now include TAD 2's measured phase difference of $53.5 \pm 1.2°$ and $\lambda_{\text{track}} = 1,910.7$ km from Table 1. Figure 11b shows a blowup of Figure 11a for the relevant region which includes these values. The hatched boxes show where the theoretical GW phase shift and calculated λ_{track} overlap with the measured phase difference and measured λ_{track} for TAD 2. Because there are regions of overlap, we conclude that TAD 2 was a GW. We also overplot the GW intrinsic period τ_{Ir} and azimuth ξ (determined from equation (24)) in Figure 11b. From the overlap regions, we estimate that GW 2 propagated southeastward with an azimuth of $\xi \sim 152$–$155°$ and had $\lambda_H = 1{,}820$–$1{,}880$ km, $|\lambda_z| = 200$–300 km, τ_{Ir} =53–55 min, and an intrinsic horizontal phase speed $c_{IH} \equiv \omega_{Ir}/k_H = 550$–$600$ m/s.

Figures 11c and 11d shows the corresponding result for TAD 4. Because there is an overlap region, we conclude that TAD 4 was a GW. We estimate that GW 4 propagated southwestward with $\xi = -144°$ to $-142°$ and had $\lambda_H = 620$–660 km, $|\lambda_z| = 1{,}450$–$1{,}850$ km, $\tau_{Ir} = 17$–18 min, and $c_{IH} = 570$–650 m/s. Figures 11e and 11f shows the corresponding result for TAD 7, which we also identified as a GW. We estimate that GW 7 propagated southeastward with $\xi = 153°$ to $154°$ and had $\lambda_H = 520$–535 km, $|\lambda_z| = 250$–400 km, τ_{Ir} =19–24 min, and $c_{IH} = 360$–470 m/s.

Figure 11 provides reasonable estimates for the intrinsic parameters of these identified GWs; however, it does not include the error in $(100\rho'/\bar{\rho}_{avg})/u'_{\text{xtrack}}$ nor does it provide 1-σ error bars for the final results. We

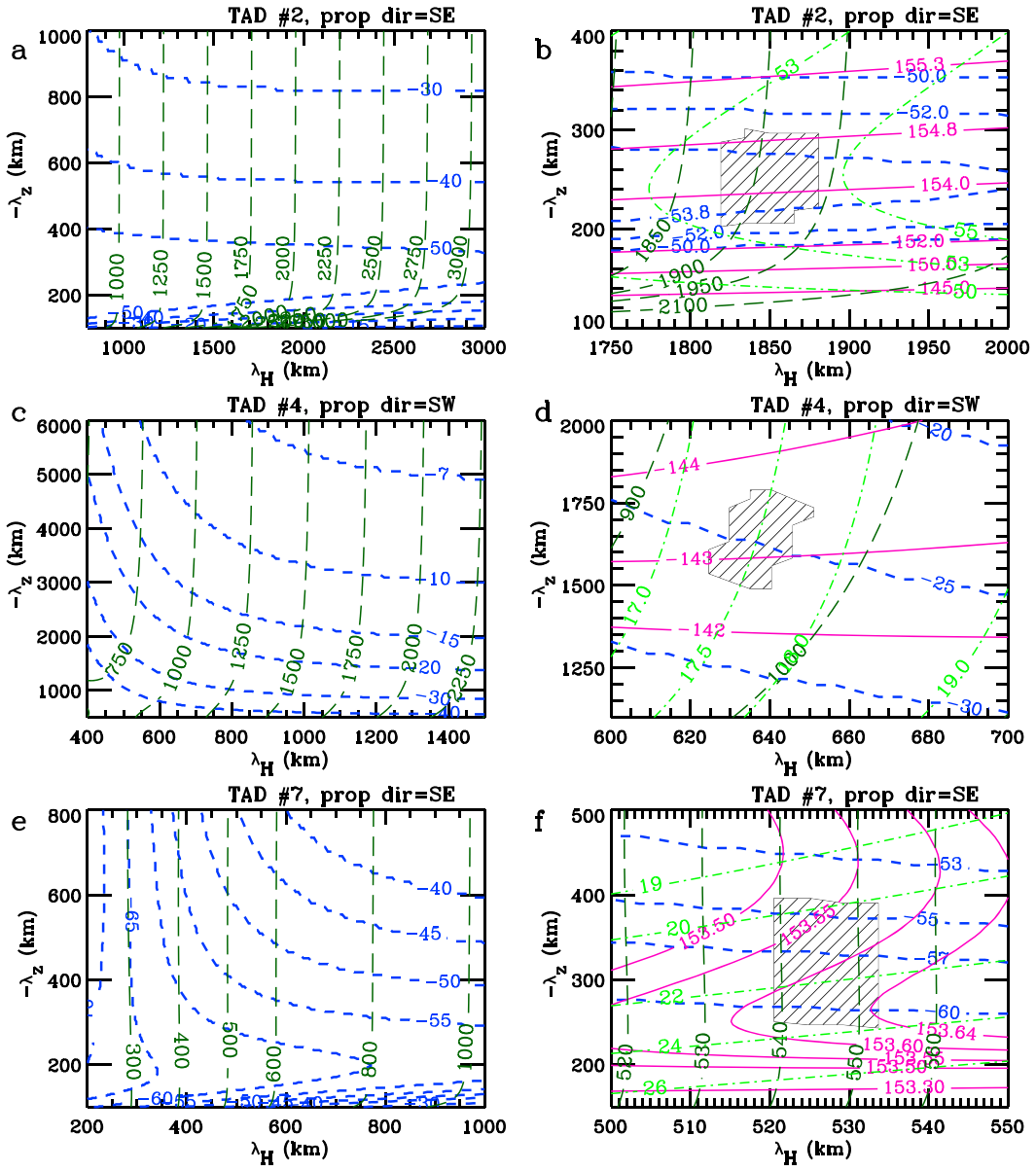

Figure 11. (a) The calculated values of λ_{track} in kilometers (long dashed dark green lines) assuming that each theoretical GW has the same amplitude ratio as that of TAD 2 (see text). The phase shift between ρ' and u'_H in degrees for the GWs (blue lines)—these are the same dashed blue lines as in Figure 10a. (b) A blowup of (a). We also overlay τ_{Ir} (dash-dot green lines, in min) and the GW azimuth ξ (solid pink lines, in degrees). The hatched boxes show the regions of overlap with the measured phase shift and measured λ_{track}. (c,d) Same as (a) and (b) but for TAD 4. (e,f) Same as (a) and (b) but for TAD 7. The gray shaded regions are for GWs with $\left|\frac{100\rho'/\bar{\rho}}{u'_H}\right| < 0.01$ s/m. GW = gravity wave; TAD = traveling atmospheric disturbance.

rectify this as follows. For each TAD, we propagate the error in $(100\rho'/\bar{\rho}_{avg})/u'_{\text{xtrack}}$ and in the phase shift to the derived GW parameters via performing Monte Carlo simulations (e.g., Anderson, 1976; Hahn & Shapiro, 1967). For each Monte Carlo TAD, we randomly select $(100\rho'/\bar{\rho}_{avg})/u'_{\text{xtrack}}$ and the phase shift assuming a normal (Gaussian) distribution with a width given by the uncertainty of each observed value. We then use the method described above to determine the intrinsic parameters of each simulated GW (if the simulated TAD is identified as a GW). The result for all of the Monte Carlo GWs are binned as functions of λ_H, λ_z, τ_{Ir}, c_{IH}, and ξ. For each of these binned functions, we fit a Gaussian to the largest peak; the best-fit Gaussian amplitudes are then the final results for λ_H, λ_z, τ_{Ir}, c_{IH}, and ξ, and the best-fit values of σ for these Gaussians are then the final results for the corresponding $1-\sigma$ errors σ_{λ_H}, σ_{λ_z}, $\sigma_{\tau_{Ir}}$, $\sigma_{c_{IH}}$, and σ_ξ, respectively. Note that we

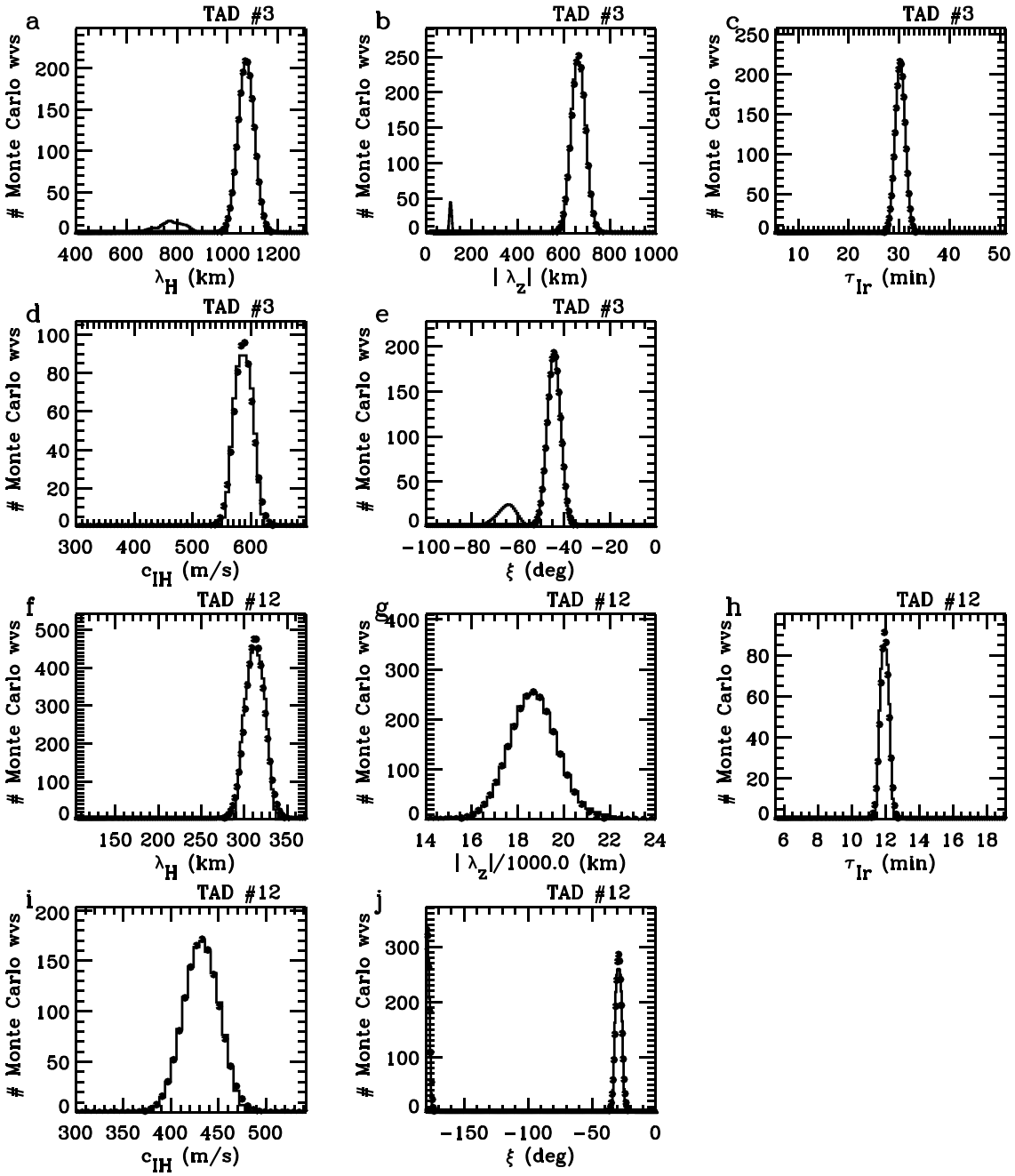

Figure 12. The Monte Carlo method used for TAD 3 to determine the best-fit intrinsic parameters for gravity wave 3 as a function of λ_H (a), $|\lambda_z|$ (b), τ_{Ir} (c), c_{IH} (d), and ξ (e). The number of Monte Carlo waves in each bin are shown on the y axis. The dots show the best-fit Gaussian. (f–j) Same as (a)–(e) but for TAD/gravity wave 12. Note that there are two best-fit Gaussians in (j) for ξ (i.e., at $\xi \sim -180°$ and 70°). TAD = traveling atmospheric disturbance.

only identify a TAD from Table 1 as a GW if (1) there are at least 10 Monte Carlo GWs in the dominant peak for each parameter, (2) $\tau_{Ir} - \sigma_{\tau_{Ir}}/2 > \tau_B$, and (3) $c_{IH} \leq c_s$ (see section 4.4). An example of this procedure for a large-scale GW is shown for TAD/GW 3 in Figures 12a–12e. Hundreds of simulated GWs are contained in each dominant peak. An example of this procedure for a medium-scale GW with $\omega_{Ir} \sim N_B$ and an extremely large $|\lambda_z|$ is shown for TAD/GW 12 in Figures 12f–12j. Although the best-fit values for λ_H, λ_z, τ_{Ir}, and c_{IH} are unambiguously determined, there are two large peaks in ξ (i.e., at $\xi \sim -180°$ and $-30°$); thus, the function for ξ is identified as a bimodal distribution. This occurs because the solution is in the vicinity of the discontinuity region in Figure 10a. Therefore, although we can positively identify TAD 12 as a GW, we cannot unambiguously determine its propagation direction.

Table 2
Derived Intrinsic Parameters for the Identified Gravity Field and Ocean Circulation Explorer Gravity Waves (GWs)

GW	λ_H (km)	$\lvert\lambda_z\rvert$ (km)	τ_{Ir} (min)	c_{IH}(m/s)	ξ (deg)
2	$1,848.8 \pm 43.7$	255.0 ± 40.2	53.69 ± 1.34	568.4 ± 16.7	153.74 ± 2.59
3	$1,074.1 \pm 32.7$	663.1 ± 31.2	30.22 ± 1.00	586.9 ± 16.1	-44.30 ± 2.91
4	653.3 ± 59.8	$1,630.0 \pm 207.0$	17.80 ± 1.35	603.4 ± 18.9	-144.31 ± 5.32
5	730.9 ± 39.9	$2,344.3 \pm 169.5$	19.26 ± 0.97	625.8 ± 15.9	—
6	502.1 ± 22.7	$1,803.3 \pm 185.1$	14.63 ± 0.50	565.5 ± 17.6	26.43 ± 3.71
7	525.6 ± 13.9	314.0 ± 95.9	22.62 ± 3.02	386.4 ± 54.2	152.87 ± 3.37
8	168.6 ± 3.9	$10,807.8 \pm 1,734.2$	11.27 ± 0.24	246.2 ± 16.0	57.64 ± 2.40
9	323.8 ± 7.9	$6,818.6 \pm 328.8$	12.02 ± 0.26	445.2 ± 16.9	-151.41 ± 2.50
10	274.7 ± 7.7	$7,810.2 \pm 340.6$	11.68 ± 0.25	387.5 ± 17.0	-55.79 ± 2.59
11	330.9 ± 49.6	$12,964.2 \pm 732.1$	12.02 ± 0.44	445.4 ± 54.7	8.68 ± 24.80
12	312.7 ± 11.5	$18,660.3 \pm 1,028.6$	11.94 ± 0.26	432.1 ± 19.0	—
14	267.1 ± 7.1	$3,692.7 \pm 354.3$	11.62 ± 0.25	378.4 ± 17.3	-22.67 ± 3.71
16	176.2 ± 5.0	$5,614.3 \pm 316.6$	11.27 ± 0.24	256.8 ± 16.3	30.61 ± 2.54
17	219.9 ± 5.4	$27,954.2 \pm 5,387.1$	11.45 ± 0.24	316.0 ± 16.4	—
18	210.7 ± 5.1	$7,032.4 \pm 516.0$	11.37 ± 0.24	304.1 ± 16.2	—
19	200.9 ± 4.7	$7,179.8 \pm 1,020.8$	11.36 ± 0.24	290.9 ± 16.2	—
20	173.4 ± 3.9	$4,921.3 \pm 443.5$	11.27 ± 0.24	253.0 ± 15.9	—

The results for all of the 17 identified GWs are shown in Table 2. From left to right, we list the GW #, λ_H, $|\lambda_z|$, τ_{Ir}, c_{IH}, and ξ. No value of ξ is listed for GWs 5, 12, and 17–20 because they had bimodal distributions in ξ. Note that TADs 1, 13, and 15 were unlikely GWs because they did not satisfy the GW dissipative polarization and dispersion relations. Those perturbations may have instead been noise, acoustic waves, and wind perturbations from local GW dissipation and momentum deposition (e.g., Vadas et al., 2014).

The GWs from Table 2 are summarized in Figure 13. Here we do not include the GWs having bimodal distributions in ξ in Figure 13d. The GWs in Figures 13a–13c have a large range of parameters: $\lambda_H \sim 170$–$1{,}850$ km, $\tau_{Ir} \sim 11$–54 min, and $c_{IH} \sim 245$–630 m/s, with the significant correlation that GWs with larger λ_H also have larger τ_{Ir} and c_{IH}. Importantly, most of the GWs have $\lambda_H < 1,100$ km and $\tau_{Ir} < 30$ min. From Figure 13d, most of the GWs have large meridional components to their propagation directions, with the majority of those propagating northwestward. This is approximately opposite to the wind direction, since according to Figure 9, the background wind was mostly eastward (and slightly southward) at $z = 277$ km with $\bar{U} = 141$ m/s, $\bar{V} = -22$ m/s, and $\sqrt{\bar{U}^2 + \bar{V}^2} \sim 143$ m/s. Note that GWs 8 and 16 are propagating significantly in the eastward direction. This is because these GWs are close to reflecting downward, with $\tau_{Ir} \sim \tau_B$; if they had propagated westward, they would have reflected downward since $\bar{U}$ increases with height (Fritts & Vadas, 2008).

An important and significant result from Table 2 and Figure 13 is that virtually all of the GWs have intrinsic horizontal phase speeds of >300 m/s. As we show in the next section, a GW cannot have an intrinsic horizontal phase speed that is larger than the sound speed of the fluid through which it is propagating. In an atmosphere dominated by diatomic molecules (which is applicable below the turbopause), the condition is that $c_{IH} \leq 0.9 c_s$ (see section 4.4). From Figure 9, the minimum sound speed below the turbopause is $c_s = 265$ m/s at $z \simeq 94$–96 km. Thus, the condition $c_{IH} \leq 0.9 c_s$ is that $c_{IH} \leq 239$m/s in order for a GW to propagate through the bottleneck near the mesopause at $z \simeq 94$–96 km. This condition is not satisfied for any of the GWs in Table 2. However, although c_H does not change significantly for a relatively fast GW as it propagates through the atmosphere, c_{IH} is highly sensitive to the change in the background horizontal wind; therefore, we must take the background wind into account before we can determine the minimum altitude that each GW could have propagated from. We do this in section 5 via reverse ray tracing.

4.4. The Largest Possible Intrinsic Horizontal Phase Speed of a GW

We now show why a GW's intrinsic horizontal phase speed can never be larger than the sound speed of the fluid through which the GW is propagating. From equation (23), the intrinsic horizontal phase speed of a

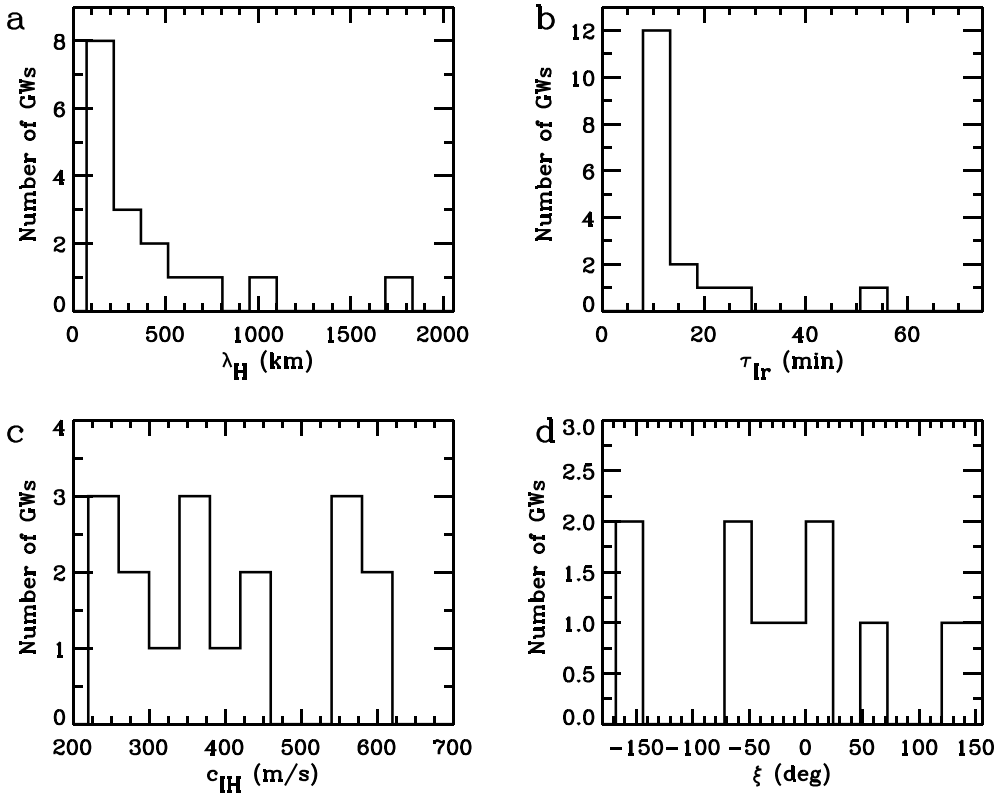

Figure 13. Histographs of the identified GWs as functions of λ_H (a), τ_{Ir} (b), c_{IH} (c), and ξ (d). GW = gravity wave.

medium- or high-frequency GW (i.e., the intrinsic phase speed along the GW propagation direction) when viscosity can be neglected is

$$c_{IH} = \frac{\omega_{Ir}}{k_H} = \frac{N_B}{\sqrt{m^2 + k_H^2 + 1/4\mathcal{H}^2}}. \tag{33}$$

The maximum intrinsic horizontal phase speed a GW can have occurs for very large $|\lambda_z|$ and λ_H, whereby the denominator of equation (33) is a minimum and is dominated by the $1/4\mathcal{H}^2$ factor. In this limit, equation (33) becomes

$$max(c_{IH}) \simeq 2\mathcal{H}N_B \tag{34}$$

(Equation (11) in Vadas & Crowley, 2010). Plugging the isothermal expressions equations (18) and (19) into equation (34), we obtain

$$max(c_{IH}) \simeq \frac{2\sqrt{\gamma - 1}}{\gamma} c_s. \tag{35}$$

When the atmosphere is dominated by diatomic molecules (i.e., below the turbopause), then $\gamma = 1.4$. When the atmosphere is dominated by monatomic molecules (i.e., at $z > 200$ km), then $\gamma = 1.667$; in between, γ increases smoothly from 1.4 to 1.667 (e.g., Vadas, 2007). Then equation (35) yields

$$max(c_{IH}) \simeq 0.90\, c_s \quad \text{(diatomic molecules)}, \tag{36}$$

$$max(c_{IH}) \simeq 0.98\, c_s \quad \text{(monatomic molecules)}. \tag{37}$$

Therefore, the maximum intrinsic horizontal phase speed a GW can have in the Earth's atmosphere is never larger than the sound speed at that location. This makes sense because an internal linear wave (that propagates via molecular interactions) should not be able to propagate faster than the sound speed.

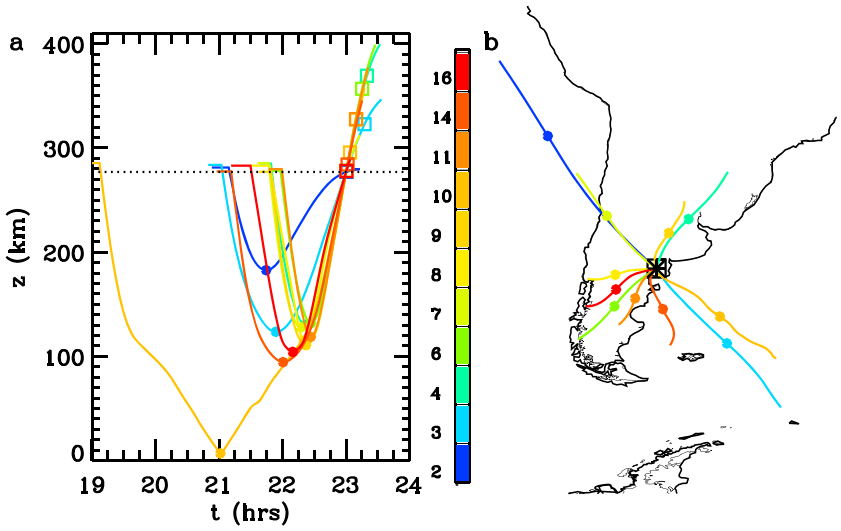

Figure 14. Ray trace results for the 11 Gravity Field and Ocean Circulation Explorer GWs from Table 2 for which ξ is known unambiguously. At 23 UT, each GW is assumed to be located at $z = 277$ km, 64° W and 40° S. The color shows the GW # (see color bar). (a) Altitude versus time. The source of each GW is located anywhere along its colored line before 23 UT. The colored dots indicate the minimum possible altitudes that each GW could have propagated from. The dotted black line shows $z = 277$ km. The colored squares show the altitude, z_{diss}, where the vertical flux of horizontal momentum (per unit mass) is maximum for each GW after 23 UT. (b) Longitudes and latitudes of each GW before 23 UT. The source of each GW is located anywhere along its colored line. The colored dots correspond to the locations of the minimum possible altitudes of the GWs (the same as the colored dots in (a)). GW = gravity wave.

5. Estimation of Source Altitudes and Locations for the GOCE GWs

We now utilize reverse ray tracing to estimate the range of possible source altitudes and locations for the identified GOCE GWs. We use a 3-D GW ray trace model that includes critical level filtering, evanescence, and realistic dissipation in the thermosphere from molecular viscosity and thermal diffusivity (e.g., Vadas, 2007; Vadas et al., 2009; Vadas & Crowley, 2017). We forward and reverse ray trace the 11 GOCE GWs from Table 2 for which ξ is known unambiguously. Although each GW was observed over a range of latitudes/longitudes (see Figure 6a), because we employed the Fast Fourier Transform to extract the GWs from the data, we lost information as to the central location of each GW along GOCE's path. Therefore, we reverse and forward ray trace each GW from an average altitude and location along GOCE's path. For the purposes of ray tracing, then, each GW is assumed to be located at $z = 277$ km, 64° W and 40° S at 23 UT. We utilize the background atmosphere shown in Figure 9 with ν given by equation (28) for $z_\mu = 220$ km and $\beta = 2$.

Figure 14a shows the ray trace results for these GWs as functions of altitude and time. The source for each GW is located anywhere along each GW's reverse ray trace "line" (i.e., prior to 23 UT). The colored dot shows the minimum possible altitude for each GW. The minima possible GW altitudes range from 7 to 183 km. Note that if a GW was created prior to the time of its colored dot, then it would have been created as a downward-propagating GW and then would have reflected upward at the time of its colored dot. On the other hand, if a GW was created after the time of its colored dot, then it would have been created as an upward-propagating GW.

In section 6, we show that on this day, MWs were propagating and attenuating over the Southern Andes at $z \sim 65$–75 km and were no longer present at $z \geq 80$ km. Therefore, the secondary GWs created by the local body forces from MW breaking would have only been created at $5 < z < 80$ km, whereas the tertiary GWs would have been created at $z > 80$ km (Vadas & Becker, 2019). From Figure 14a, since 10 of these GWs were created at $z \geq 94$ km, they were therefore likely tertiary GWs. The eleventh one, GW 10, could have been created at $z < 80$ km because it had a minimum source altitude of $z = 7$ km and therefore could have potentially been a primary GW (given the error in the ray tracing). However, this GW reflected upward at $z = 7$ km whereby $m = 0$. At $z = 7$ km, $\bar{U} = 23$ m/s, $\bar{V} = 0$ and $4\pi\mathcal{H} \simeq 65$km from Figure 9. Since $\lambda_{\text{H}} \geq 176$ km from Table 2, $1/4\mathcal{H}^2 >> k_H^2$. Therefore, at the reflection point, $c_{IH} \simeq 2\mathcal{H}N_B$ from equation (33).

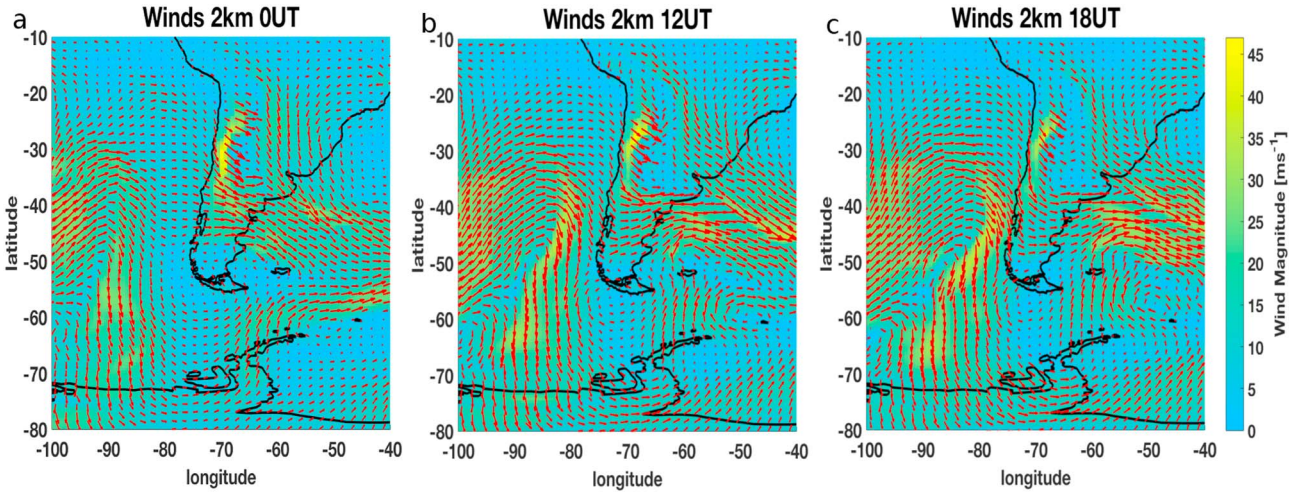

Figure 15. Horizontal wind at $z = 2$ km from Modern-Era Retrospective analysis for Research and Applications-2 at 0, 12, and 18 UT on 5 July 2010. The arrows show the wind direction. The length of each arrow is proportional to its magnitude, shown in color (in m/s; see color bar).

Using $c_s = 311$m/s from Figure 9, this implies that the GW's intrinsic horizontal phase speed at $z = 7$ km (as it reflected) was $c_{IH} = 0.9c_s = 280$m/s from equation (36). To our knowledge, there is no known winter-time source of primary GWs in the troposphere with such large phase speeds. Therefore, GW 10 was likely a secondary or tertiary GW.

Figure 14a also shows the forward ray trace results for each GW. We calculate each GW's momentum flux using Equation (50) from Vadas and Fritts (2009). A square marks the location where each GW's vertical flux of horizontal momentum (per unit mass), $\overline{u'w'}$, is maximum (dubbed "$z_{\rm diss}$"). Above this altitude, $\overline{u'w'}$ decreases rapidly in altitude because of molecular viscosity (Vadas, 2007). We see that most of the GWs dissipate within ~30 min after GOCE observed them at altitudes of $z_{\rm diss} \sim 277$–370 km.

Figure 14b shows the reverse ray trace results for each GW as functions of longitude and latitude (i.e., prior to 23 UT). The source of each GW is located anywhere along its colored line. The colored dots correspond to the same times/locations as the colored dots in Figure 14a, which indicates the location where each GW could have had its minimum altitude (if it was created at or before the corresponding time in Figure 14a). Because we chose to reverse ray trace each GW from 64° W and 40° S at 23 UT (even though each GW was observed over a range of latitudes/longitudes; see Figure 6a), all of the colored lines converge at 64° W and 40° S at 23 UT in Figure 14b. We see that the possible source locations for these GWs range over a large horizontal area: from over South America to over the Atlantic and Pacific Oceans. Thus, the possible source locations for these GWs span latitudes of 10–65° S and longitudes of 45–85° W. This is consistent with the source locations for the secondary and tertiary GWs generated from MW breaking over the Southern Andes (Vadas & Becker, 2019).

6. MWs Over the Southern Andes

Because the GOCE hot spot GWs are located over the Southern Andes Mountains, it is reasonable to suspect that orographic GW sources are linked to these hot spot GWs. Therefore, we now determine if MWs were created 5 July 2010, and if so, how far they propagated in the atmosphere before attenuating (if possible).

Figure 15 shows the horizontal wind from Modern-Era Retrospective analysis for Research and Applications-2 on 5 July 2010 at 0, 12, and 18 UT. A synoptic-scale weather system is visible over and around the South American continent. These baroclinic Rossby waves move eastward in vortex-like patterns. Below 20° S, the wind patterns are complex. There is a strong ~40 m/s southeastward wind on the west side of the Southern Andes mountain range at 22–45° S at 0, 12, and 18 UT. There is also ~20 m/s eastward winds at 0 and 18 UT and a ~20 m/s northeastward wind at 6 UT (not shown) and at 12 UT on central and eastern sides of the continent. This latter wind is quite variable and has a significant northward meridional component at 6 and 12 UT. Note that the mountain range extends across the entire continent longitudinally at

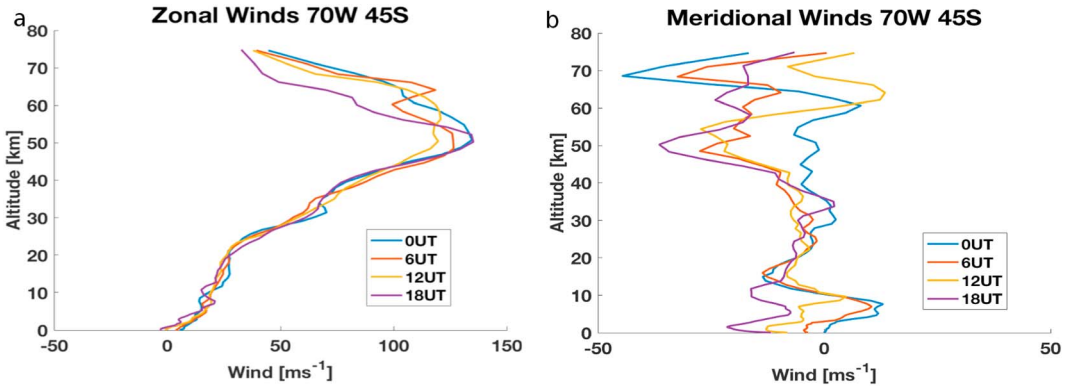

Figure 16. Zonal (a) and meridional wind (b) at 0, 6, 12, and 18 UT at 45° S and 70° W on 5 July 2010 from Modern-Era Retrospective analysis for Research and Applications-2.

the location where the wind is northeastward (∼50° S). These wind amplitudes are large-enough to excite MWs. Figure 16 shows vertical profiles of the zonal and meridional wind at 0, 6, 12, and 24 UT. The winter stratospheric polar jet is very strong, with maxima eastward winds of ∼120–140 m/s at $z \sim 50$–65 km. This allows for the vertical propagation of strong MWs into the stratosphere and lower mesosphere.

We now look for MWs in measurements from the AIRS instrument on the AQUA satellite. In particular, we examine the radiance from the CO_2 15-μm emission, which is centered at $z \sim 40$ km and has a full-width-half-max of ∼12 km. Perturbations of the radiance can reveal GWs (such as MWs) if $|\lambda_z| \geq 12$ km (Alexander & Barnett, 2007; Gong et al., 2012). Although MWs typically have $|\lambda_z| < 10$ km in the troposphere, $|\lambda_z|$ can increase significantly if the MWs propagate into an oppositely directed wind that increases with altitude, because $|\lambda_z|$ is proportional to the background wind (e.g., Alexander & Teitelbaum, 2007). For example, MWs excited by an eastward wind propagate westward in the intrinsic reference frame (although they are stationary in the ground-based reference frame). If the eastward wind increases in the stratosphere (e.g., in the polar night jet), then $|\lambda_z|$ increases significantly in the lower to middle stratosphere (e.g., Vadas & Becker, 2018); if $|\lambda_z| \geq 12$ km in the CO_2 15-μm emission layer, then the MW can be observed by AIRS. Additionally, the AIRS radiances are sensitive to GWs with λ_H as small as ∼80 km (Alexander & Teitelbaum, 2007). Orographic hot spots have been observed with AIRS (e.g., Alexander & Grimsdell, 2013; Hoffmann et al., 2016).

We calculate the AIRS radiances using the methods from Alexander and Barnett (2007). Figure 17 shows granule maps of the radiance perturbations on 5 July 2010 at $5 - 6.8$ UT and $18.5 - 20.3$ UT. A complicated mix of prominent wave perturbations is seen with many different horizontal wavelengths and orientations.

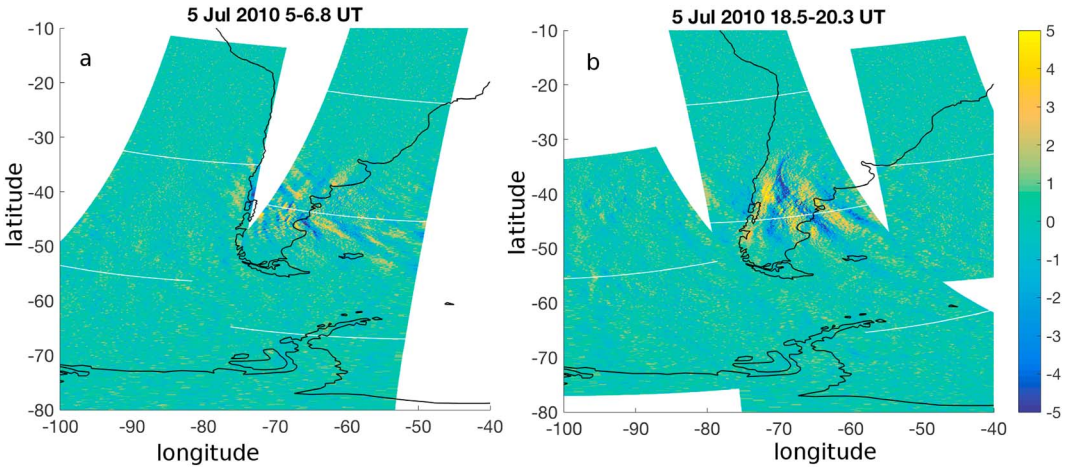

Figure 17. Atmospheric Infrared Sounder data on 5 July 2010 at (a) 5–6.8 UT and (b) 18.5–20.3 UT. The radiance perturbations from the CO_2 15-μm emission are shown in colors (in mW/m^2 cm/sr).

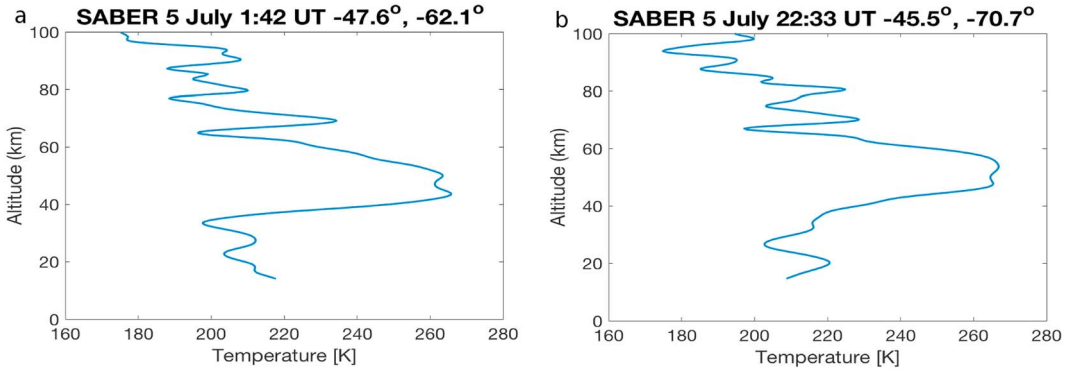

Figure 18. Temperature profiles from SABER on 5 July 2010. (a) 1:42 UT at 47.6° S and 62.1° W. (b) 22:33 UT at 45.5° S and 70.7° W. SABER = Sounding of the Atmosphere using Broadband Emission Radiometry.

In both panels, waves are prominent having phase lines that are nearly parallel to the Southern Andes mountain range on the western side of South America (i.e., southwest to northeast). These waves are confined to the eastern side of the mountain range and have $\lambda_H \sim 275$ km at 35–41° S and 65–70° W and have $\lambda_H \sim 100$ km at 41–45° S and 66–72° W. There are also larger-scale waves with phase lines oriented northwest to southeast having $\lambda_H \sim 440$ km at 40–50° S and 72–76° W; these latter waves are more prominent at 18.5 – 20.3 UT. Finally, there are very faint waves with phase lines that are oriented northwest to southeast having $\lambda_H \sim 140$ km at 50° S and 72° W.

We now argue that the dominant waves in Figure 17 are likely MWs. First, we note from Figure 16 that the polar night jet is quite strong and eastward; therefore, $|\lambda_z|$ likely increased significantly for the MWs, thereby allowing them to be detected by AIRS. Next we examine the orientation of the wave phase lines with the mountain range and wind direction. The waves parallel to the Southern Andes and just east of the mountain range (with $\lambda_H \sim 100$ and 275 km) are most likely MWs, because the wind there is steady and southeastward, roughly perpendicular to the mountain chain. It is possible that the GWs at 45° S have $\lambda_H \sim 100$ km because the mountain chain is narrower there. The other prominent waves have phase lines oriented northwest to southeast (with $\lambda_H \sim 440$ km). These phase lines are roughly perpendicular to the strong northeastward wind at 6 and 12 UT on central and eastern side of the continent. At this location (~50° S), the mountain range extends the full longitudinal width of the continent. Therefore, these latter waves are also likely MWs, created by the strong northeastward wind seen in Figure 15.

We now examine data from SABER. This instrument provides temperature profiles from the lower stratosphere up to the thermosphere (Remsberg et al., 2008). We find that GWs were present throughout the day on 5 July 2010. Figure 18 shows two example profiles at 1:42 and 22:33 UT at locations where strong MW activity occurred in Figure 17. Significant GW perturbations with $\lambda_z \sim 4$–6 km and $T' \sim 20$ K occur at $z \sim$ 60–80 km, indicating strong GW activity. These temperature perturbations are quite similar to the SABER MW temperature perturbations observed over the South Island of New Zealand; in that case, the perturbations agreed very well with the MW temperature perturbations measured by simultaneous ground-based lidar instruments (Bossert et al., 2015). Because of the strong MW activity in the AIRS data on 5 July 2010 (see Figure 17) as well as the similarity to the results of Bossert et al. (2015), it is likely that the GW perturbations at $z \sim 60$–80 km in Figure 18 are due to MWs. We assume that this is the case here.

Because the MW amplitude peaks at $z \sim 70$ km in Figure 18 and decreases above, it is likely that the MW attenuates at $z > 70$ km. Indeed, the MW is not visible at $z \geq 80$ km. We determine if this MW became convectively unstable using equation (1). Because $c_H \sim 0$ for MWs, and the background wind over the mountains was mainly eastward, equation (1) becomes

$$|u'_H| \sim (0.7 - 1.0)\ |\bar{U}|. \tag{38}$$

From Figure 16, the background zonal wind decreases rapidly above $z > 60$ km where the polar night jet "ends," with $|\bar{U}| \sim 45$ m/s at $z \sim 70$ km. The polarization relation which relates T' and u'_H for a

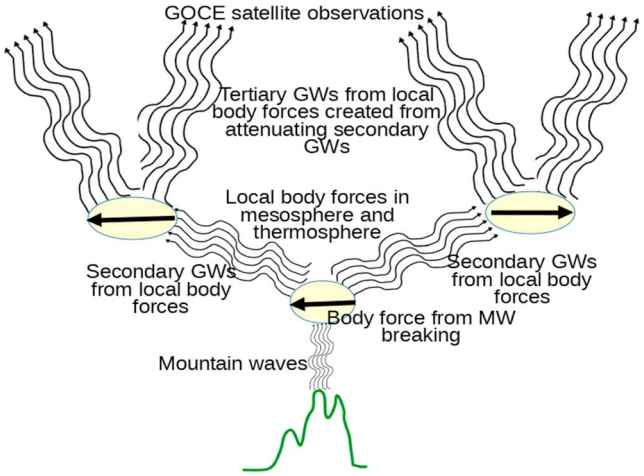

Figure 19. Schematic showing the multistep coupling mechanism for the transfer of momentum and energy via MW breaking to secondary to tertiary GWs. MWs are excited from orographic forcing. Local body forces are created where the MWs break and attenuate (horizontal black arrows). Larger-scale secondary GWs are excited by these body forces. Local body forces are created where these secondary GWs attenuate, which excite tertiary GWs. Only the upward-propagating secondary and tertiary GWs are shown here for clarity. (Not to scale.) GOCE = Gravity Field and Ocean Circulation Explorer; GW = gravity wave; MW = mountain wave.

midfrequency GW below the turbopause is (equations (11) and (12) with $\nu \sim 0$, $\lambda_H \gg |\lambda_z|$, $|\lambda_z| \ll 4\pi\mathcal{H}$ and $c_s \to \infty$; e.g., Equation (44) of Vadas et al., 2018)

$$|u'_H| \sim \frac{g}{N_B}\left|\frac{T'}{\bar{T}}\right|, \tag{39}$$

where we have used equations (17), (18), and (23). Using $T' \sim 20$ K and $\bar{T} \sim 210$ K from Figure 18 and $N_B = 0.02$rad/s, $|u'_H| \sim 47$ m/s. Therefore, this MW became convectively unstable at $z \sim 70$ km from equation (38). This result agrees very well with the MW amplitude decreasing at $z > 70$ km in Figure 18. Because the MW broke/attenuated at $z > 70$ km, it deposited its momentum and energy into the background flow over a spatially localized region. Such a deposition would have resulted in the excitation of larger-scale secondary GWs (Vadas et al., 2018).

7. Discussion

We now discuss the possibility that orographic forcing was the source of the GOCE hot spot GWs. As we showed in this paper, MWs broke and attenuated over the Southern Andes at $z \sim 70$–80 km on 5 July 2010. These nonlinear processes would have created vortical motions and small-scale secondary GWs (e.g., Bacmeister & Schoeberl, 1989; Bossert et al., 2017; Chun & Kim, 2008). During the cascade to turbulence, GW momentum would have been deposited into the background flow, thereby creating local body forces (i.e., horizontal accelerations). These body forces would have excited larger-scale secondary GWs, similar to the secondary GWs recently studied via modeling and observations (Becker & Vadas, 2018; Vadas & Becker, 2018; Vadas et al., 2018). Some of these secondary GWs would have dissipated below the turbopause, thereby creating local body forces there (Becker & Vadas, 2018). Many of these secondary GWs would have propagated into the thermosphere (Vadas, 2007), because the secondary GW spectrum is quite broad and contains GWs with large $|\lambda_z|$ (Vadas et al., 2018). In the thermosphere, these secondary GWs would have dissipated from molecular viscosity (Vadas, 2007) or from breakdown into turbulence (Lund & Fritts, 2012); either situation would have resulted in the secondary GWs depositing their momentum into the background flow, which would have resulted in the creation of local body forces. All of the body forces created from the attenuation of secondary GWs would have excited *tertiary* GWs by the same mechanism that excited the secondary GWs (see Vadas et al., 2003). Figure 19 sketches this mechanism. Using a high-resolution GW-resolving model, Vadas and Becker (2019) demonstrates in a companion paper that tertiary GWs are indeed excited in the mesosphere and thermosphere over the Southern Andes where the secondary GWs dissipate. In that study, the tertiary GWs were excited at $z \sim 80$ to 130 km.

The hypothesis that the wintertime quiet-time hot spot GWs in the middle thermosphere over the Southern Andes are tertiary (or higher-order) GWs is also supported by a recent study by Park et al. (2014). These authors found that the amplitudes of the TAD density perturbations from the CHAMP satellite were twice as large during solar minimum (~1.2%) than during solar maximum (~0.6%). If some of these TADs were GWs, then this result is consistent with these GWs being created by thermospheric body forces, because ν increases much more rapidly in altitude during solar minimum than solar maximum, thereby causing the resulting body force to have a smaller vertical extent and a 2–3 times larger amplitude during solar minimum than during solar maximum (Vadas & Fritts, 2006). Because the amplitude of a GW created by a body force is proportional to the force's amplitude (Vadas et al., 2003), the amplitudes of these excited tertiary (or higher-order) GWs would be 2–3 times larger during solar minimum than during solar maximum (Vadas et al., 2014). This is consistent with these CHAMP observations.

8. Conclusions

In this paper, we investigated the quiet-time, hot spot TADs observed by GOCE at $z = 277$ km on 5 July 2010 at 23 UT as GOCE overpassed the Southern Andes. Our motivation for this study was to identify which hot

spot TADs were GWs and to determine the intrinsic properties and possible sources of the identified hot spot GOCE GWs.

We first extracted the TADs having the 20 largest values of λ_{track} from the in situ density and cross-track wind perturbations using discrete Fourier transforms. We then searched parameter space to determine if each TAD was a GW using GW dissipative theory that includes realistic viscosity in the thermosphere. We found that 17 of these TADs were GWs, with $\lambda_H = 170$–$1{,}850$ km, $\tau_{Ir} = 11$–54 min, $c_{IH} = 245$–630 m/s, and $\rho'/\bar{\rho} \sim 0.03$–$7\%$. Most of the GWs had $\lambda_H < 1{,}100$ km and $\tau_{Ir} < 30$ min. We unambiguously determined the propagation direction for 11 of these GWs and found that most had large meridional components to their propagation directions.

We then reverse ray traced these identified hot spot GOCE GWs. We found that the source for 10 of them was in the mesosphere or thermosphere and that the source for the other GW was at $z \geq 7$ km. Because this latter GW had an intrinsic phase speed of $c_{IH} \simeq 280$m/s at $z = 7$ km, and because there are no known primary GWs with such large phase speeds at the Earth's surface, we argued that this GOCE GW was either a secondary or tertiary GW. Because the former 10 GOCE GWs were created at $z \geq 94$ km, we argued that they were tertiary GWs. Here the secondary GWs would have been generated at $z \sim 5$–80 km and the tertiary (and higher-order) GWs would have been generated at $z > 80$ km. This result strongly suggests that the quiet-time GOCE hot spot GWs over the Southern Andes cannot be reproduced by conventional global circulation models that only launch parameterized GWs from the troposphere or lower stratosphere (e.g., Yigit & Medvedev, 2010); instead, GW-resolving models that adequately account for the intermittency of the local body forces from primary and secondary GWs are needed.

Our ray trace results also found that the possible source locations for the identified GOCE hot spot GWs include 10–65° S and 45–85° W over and surrounding South America. Using AIRS and SABER data, we showed that MWs were present over the Southern Andes on 5 July 2010. We also showed that they likely saturated from convective instability at $z \sim 70$–75 km that day and that they were not present at $z \geq 80$ km. This is consistent with Trinh et al. (2018), who used SABER data to show that during June 2010–2013, the GW hot spot over the Southern Andes weakened considerably at $z \sim 75$ km and was completely absent at $z = 80$–90 km (their Figure 2).

Given the discussion in section 7, we suggest that 10 of the identified GOCE hot spot GWs were likely tertiary (or higher-order) GWs caused by MW breaking and that the other GW was likely a secondary or tertiary (or higher-order) GW caused by MW breaking. This multistep coupling mechanism from orographic MW generation in the winter troposphere to tertiary (or higher-order) GWs in the thermosphere results in the significant transfer of momentum and energy from the troposphere to the thermosphere (Vadas & Becker, 2019). Future works will investigate this multistep coupling mechanism further.

Acknowledgments
S. L. V. was supported by NSF grants AGS-1832988, AGS-1552315, AGS-1452329, and AGS-1242897. J. Y. was supported by NSF grants AGS-1651394 and AGS-1834222, and NASA's Small Explorers Program AIM under contract NAS5-03132. K. B. was supported by NSF grant AGS-1822585. E. B. was supported by the Collaborative Research Centre TRR 181 (subproject T1) funded by the German Research Foundation. Data from MERRA-2 is available online (https://gmao.gsfc.nasa.gov/reanalysis/MERRA-2/). Data from MSIS is available online (https://ccmc.gsfc.nasa.gov/modelweb/models/nrlmsise00.php). Data from HWM is available in "Supporting Information" of Drob et al. (2015; https://agupubs.onlinelibrary.wiley.com/doi/10.1002/2014EA000089). The GOCE data access is https://earth.esa.int/web/guest/-/goce-data-access-7219, and the direct download link for GOCE data is http://eo-virtual-archive1.esa.int/GOCE-Thermosphere.html; data from AIRS and MERRA-2 are available online (https://disc.gsfc.nasa.gov/SSW/#keywords=), and data from SABER are available online (http://saber.gats-inc.com/data.php). The model data shown in this paper are available via NWRA's website (https://www.cora.nwra.com/vadas/Vadas_etal_GOCEJGR_2019_files/).

References

Alexander, M. J., & Barnett, C. (2007). Using satellite observations to constrain parameterizations of gravity wave effects for global models. *Journal of the Atmospheric Sciences*, *64*, 1652–1665. https://doi.org/10.1175/JAS387.1

Alexander, M. J., Gille, J., Cavanaugh, C., Coffey, M., Craig, C., Eden, T., et al. (2008). Global estimates of gravity wave momentum flux from High Resolution Dynamics Limb Sounder Observations. *Journal of Geophysical Research*, *113*, D15S18. https://doi.org/10.1029/2010JD008807

Alexander, S. P., & Grimsdell, A. (2013). Seasonal cycle of orographic gravity wave occurrence above small islands in the Southern Hemisphere: Implications for effects on the general circulation. *Journal of Geophysical Research: Atmospheres*, *118*, 11,589–11,599. https://doi.org/10.1002/2013JD020526

Alexander, M. J., & Teitelbaum, H. (2007). Observation and analysis of a large amplitude mountain wave event over the Antarctic peninsula. *Journal of Geophysical Research*, *112*, D21103. https://doi.org/10.1029/2006JD008368

Anderson, G. M. (1976). Error propagation by the Monte Carlo method in geochemical calculations. *Geochimica et Cosmochimica Acta*, *40*(12), 1533–1538.

Bacmeister, J. T., & Schoeberl, M. R. (1989). Breakdown of vertically propagating two-dimensional gravity waves forced by orography. *Journal of the Atmospheric Sciences*, *46*, 2109–2134.

Banks, P. M., & Kockarts, G. (1973). *Aeronomy part B*, (pp. 355). New York: Academic Press.

Becker, E., & Vadas, S. L. (2018). Secondary gravity waves in the winter mesosphere: Results from a high-resolution global circulation model. *Journal of Geophysical Research: Atmospheres*, *123*, 2605–2627. https://doi.org/10.1002/2017JD027460

Bossert, K., Fritts, D. C., Pautet, P.-D., Williams, B. P., Taylor, M. J., Kaifler, B., et al. (2015). Momentum flux estimates accompanying multiscale gravity waves over Mount Cook, New Zealand, on 13 July 2014 during the DEEPWAVE campaign. *Journal of Geophysical Research: Atmospheres*, *120*, 9323–9337. https://doi.org/10.1002/2015JD023197

Bossert, K., Kruse, C. G., Heale, C. J., Fritts, D. C., Williams, B. P., Snively, J. B., et al. (2017). Secondary gravity wave generation over New Zealand during the DEEPWAVE campaign. *Journal of Geophysical Research: Atmospheres*, *122*, 7834–7850. https://doi.org/10.1002/2016JD026079

Bruinsma, S. (2013). Air density and wind retrieval using GOCE data. Validation Rep. European Space Agency (ESA) AO/1-6367/10/NL/AF. Available at, https://earth.esa.int/web/guest/missions/esa-operational-missions/goce/goce-thermospheric-data

Bruinsma, S. L., Doornbos, E., & Bowman, B. R. (2014). Validation of GOCE densities and thermosphere model evaluation. *Advances in Space Research*, *54*, 576–585. https://doi.org/10.1016/j.asr.2014.04.008

Chun, H.-Y., & Kim, Y.-H. (2008). Secondary waves generated by breaking of convective gravity waves in the mesosphere and their influence in the wave momentum flux. *Journal of Geophysical Research*, *113*, D23107. https://doi.org/10.1029/2008JD009792

Dhadly, M. S., Emmert, J. T., Drob, D. P., Conde, M. G., Doornbos, E., Shepherd, G. G., & Ridley, A. J. (2017). Seasonal dependence of geomagnetic active-time northern high-latitude upper thermospheric winds. *Journal of Geophysical Research: Space Physics*, *122*, 739–754. https://doi.org/10.1002/2017JA024715

Doornbos, E. (2016). Air density and wind retrieval using GOCE data. European Space Agency (ESA) AO/1-6367/10/NL/AF, Version 1.5 Data Set User Manual. Available athttps://earth.esa.int/web/guest/missions/esa-operational-missions/goce/goce-thermospheric-data

Doornbos, E., Bruinsma, S. L., Fritsche, B., Koppenwallner, G., Visser, P., van den IJssel, J., & de Teixeira de Encarnacao, J. (2014). Air density and wind retrieval using GOCE data (*Final Rep.*): European Space Agency (ESA) contract 4000102847/NL/EL. Available athttps://earth.esa.int/web/guest/missions/esa-operational-missions/goce/goce-thermospheric-data

Doornbos, E., Visser, P., Koppenwallner, G., & Fritsche, B. (2013). Air density and wind retrieval using GOCE data (*Validation Rep.*): European Space Agency (ESA) AO/1-6367/10/NL/AF, Algorithm Theoretical Basis Document. Available at https://earth.esa.int/web/guest/missions/esa-operational-missions/goce/goce-thermospheric-data

Drob, D. P., Emmert, J. T., Meriwether, J. W., Makela, J. J., Doornbos, E., Conde, M., et al. (2015). An update to the Horizontal Wind Model (HWM): The quiet time thermosphere. *Earth and Space Science*, *2*, 301–319. https://doi.org/10.1002/2014EA000089

Eckermann, S. D, Broutman, D., Ma, J., Doyle, J. D., Pautet, P.-D., Taylor, M. J., et al. (2016). Dynamics of orographic gravity waves observed in the mesosphere over the Auckland islands during the deep propagating gravity wave experiment (DEEPWAVE). *Journal of the Atmospheric Sciences*, *73*. https://doi.org.10.1175/JAS-D-16-0059.1

Ern, M., Preusse, P., Alexander, M. J., & Warner, C. D. (2004). Absolute values of gravity wave momentum flux derived from satellite data. *Journal of Geophysical Research*, *109*, D20103. https://doi.org/10.1029/2004JD004752

Ern, M., Preusse, P., Gille, J. C., Hepplewhite, C. L., Mlynczak, M. G., Russell, J. M. III, & Riese, M. (2011). Implications for atmospheric dynamics derived from global observations of gravity wave momentum flux in stratosphere and mesosphere. *Journal of Geophysical Research*, *116*, D19107. https://doi.org/10.1029/2011JD015821

Forbes, J. M., Bruinsma, S. L., Doornbos, E., & Zhang, X. (2016). Gravity wave-induced variability of the middle thermosphere. *Journal of Geophysical Research: Space Physics*, *121*, 6914–6923. https://doi.org/10.1002/2016JA022923

Fritts, D. C., & Alexander, M. J. (2003). Gravity wave dynamics and effects in the middle atmosphere. *Reviews of Geophysics*, *41*(1), 1003. https://doi.org/10.1029/2001RG000106

Fritts, D. C., Smith, R. B., Taylor, M. J., Doyle, J. D., Eckermann, S. D., Dörnbrack, A., et al. (2016). The deep propagating gravity wave experiment (DEEPWAVE): An Airborne and ground-based exploration of gravity wave propagation and effects from their sources throughout the lower and middle atmosphere. *Bulletin of the American Meteorological Society*, *97*, 425–453. https://doi.org/10.1175/BAMS-D-14-00269.1

Fritts, D. C., & Vadas, S. L. (2008). Gravity wave penetration into the thermosphere: Sensitivity to solar cycle variations and mean winds. *Annales Geophysicae*, *26*, 3841–3861. https://doi.org/10.5194/angeo-26-3841-2008

Gong, J., Wu, D. L., & Eckermann, S. D. (2012). Gravity wave variances and propagation derived from AIRS radiances. *Atmospheric Chemistry and Physics*, *12*, 1701–1720. https://doi.org/10.5194/acp-12-1701-2012

Gross, S. H., Reber, C. A., & Huang, F. T. (1984). Large-scale waves in the thermosphere observed by the AE-C satellite. *IEEE Transactions on Geoscience and Remote Sensing*, *GE-22*, 340–352.

Hahn, G. J., & Shapiro, S. S. (1967). *Statistical models in engineering, Wiley series on systems engineering and analysis*. New York, NY: Wiley.

Heale, C. J., Bossert, K., Snively, J. B., Fritts, D. C., Pautet, P.-D., & Taylor, M. J. (2017). Numerical modeling of a multiscale gravity wave event and its airglow signatures over Mount Cook, New Zealand, during the DEEPWAVE campaign. *Journal of Geophysical Research: Space Phyisics*, *122*, 846–860. https://doi.org/10.1002/2016JD025700

Hedin, A. E. (1991). Extension of the MSIS thermosphere model into the middle and lower atmosphere. *Journal of Geophysical Research*, *96*, 1159.

Hines, C. O. (1960). Internal atmospheric gravity waves at ionospheric heights. *Canadian Journal of Physics*, *38*, 1441–1481.

Hoffmann, L., & Alexander, M. J. (2010). Occurrence frequency of convective gravity waves during the North American thunderstorm season. *Journal of Geophysical Research*, *115*, D20111. https://doi.org/10.1029/2010jd014401

Hoffmann, L., Grimsdell, A. W., & Alexander, M. J. (2016). Stratospheric gravity waves at Southern Hemisphere orographic hotspots: 2003-2014 AIRS/Aqua observations. *Atmospheric Chemistry and Physics*, *16*, 9381–9397. https://doi.org/10.5194/acp-16-9381-2016

Hoffmann, L., Xue, X., & Alexander, M. J. (2013). A global view of stratospheric gravity wave hotspots located with Atmospheric Infrared Sounder observations. *Journal of Geophysical Research: Atmospheres*, *118*, 416–434. https://doi.org/10.1029/2012JD018658

Innis, J. L., & Conde, M. (2002). Characterization of acoustic-gravity waves in the upper thermosphere using Dynamics Explorer 2 Wind and Temperature Spectrometer (WATS) and Neutral Atmosphere Composition Spectrometer (NACS) data. *Journal of Geophysical Research*, *A12*(1418), 107. https://doi.org/10.1029/2002JA009370

Jiang, J. H., Eckermann, S. D., Wu, D. L., & Wang, D. Y. (2006). Inter-annual variation of gravity waves in the Arctic and Antarctic winter middle atmosphere. *Advances in Space Research*, *38*, 2418–2423.

Jiang, J. H., Wu, D. L., Eckermann, S. D., & Ma, J. (2003). Mountain waves in the middle atmosphere: Microwave limb sounder observations and analyses. *Advances in Space Research*, *32*(5), 801–806. https://doi.org/lO.l016/S0273-1177(03)00402-2

Larsen, M. F. (2002). Winds and shears in the mesosphere and lower thermosphere: Results from four decades of chemical release wind measurements. *Journal of Geophysical Research*, *107*(A8), 1215. https://doi.org/10.1029/2001JA000218

Larsen, M. F., Liu, A. Z., Bishop, R. L., & Hecht, J. H. (2003). TOMEX: A comparison of lidar and sounding rocket chemical tracer wind measurements. *Geophysical Research Letters*, *30*(7), 1375. https://doi.org/10.1029/2002GL015678

Lindzen, R. S. (1981). Turbulence and stress owing to gravity wave and tidal breakdown. *Journal of Geophysical Research*, *86*(C10), 9707–9714.

Liu, H., Pedatella, N., & Hocke, K. (2017). Medium-scale gravity-wave activity in the bottomside F region in tropical regions. *Geophysical Research Letters*, *44*, 7099–7105. https://doi.org/10.1002/2017GL073855

Lund, T. S., & Fritts, D. C. (2012). Numerical simulation of gravity wave breaking in the lower thermosphere. *Journal of Geophysical Research*, *117*, D21105. https://doi.org/10.1029/2012JD017536

Marks, C. J., & Eckermann, S. D. (1995). A three-dimensional nonhydrostatic ray-tracing model for gravity waves: Formulation and preliminary results for the middle atmosphere. *Journal of the Atmospheric Sciences*, *52*, 1959–1984.

Nicolls, M. J., Vadas, S. L., Aponte, N., & Sulzer, M. P. (2014). Horizontal wave parameters of daytime thermospheric gravity waves and E-Region neutral winds over Puerto Rico. *Journal of Geophysical Research: Atmospheres*, *119*, 576–600. https://doi.org/10.1002/2013JA018988

Park, J., Lühr, H., Lee, C., Kim, Y. H., Jee, G., & Kim, J.-H. (2014). A climatology of medium-scale gravity wave activity in the midlatitude/low-latitude daytime upper thermosphere as observed by CHAMP. *Journal of Geophysical Research: Space Physics*, *119*, 2187–2196. https://doi.org/10.1002/2013JA019705

Remsberg, E. E., Marshall, B. T., Garcia-Comas, M., Krueger, D., Lingenfelser, G. S., Martin-Torres, J., et al. (2008). Assessment of the quality of the version 1.07 temperature-versus-pressure profiles of the middle atmosphere from TIMED/SABER. *Journal of Geophysical Research*, *113*, D17101. https://doi.org/10.1029/2008JD010013

Trinh, Q. T., Ern, M., Doornbos, E., Preusse, P., & Riese, M. (2018). Satellite observations of middle atmosphere-thermosphere vertical coupling by gravity waves. *Annales Geophysicae*, *36*, 425–444. https://doi.org/10.5194/angeo-36-425-2018

Vadas, S. L. (2007). Horizontal and vertical propagation and dissipation of gravity waves in the thermosphere from lower atmospheric and thermospheric sources. *Journal of Geophysical Research*, *112*, A06305. https://doi.org/10.1029/2006JA011845

Vadas, S. L., & Becker, E. (2018). Numerical modeling of the excitation, propagation, and dissipation of primary and secondary gravity waves during wintertime at McMurdo Station in the Antarctic. *Journal of Geophysical Research: Atmospheres*, *123*, 9326–9369. https://doi.org/10.1029/2017JD027974

Vadas, S. L., & Becker, E. (2019). Numerical modeling of tertiary gravity waves from mountain wave breaking over the Southern Andes. *Journal of Geophysical Research: Space Physics*. https://doi.org.10.1029/2019JA026694

Vadas, S. L., & Crowley, G. (2010). Sources of the traveling ionospheric disturbances observed by the ionospheric TIDDBIT sounder near Wallops Island on October 30, 2007. *Journal of Geophysical Research*, *115*, A07324. https://doi.org/10.1029/2009JA015053

Vadas, S. L., & Crowley, G. (2017). Neutral wind and density perturbations in the thermosphere created by gravity waves observed by the TIDDBIT sounder. *Journal of Geophysical Research: Space Physics*, *122*, 6652–6678. https://doi.org/10.1002/2016JA023828

Vadas, S. L., & Fritts, D. C. (2005). Thermospheric responses to gravity waves: Influences of increasing viscosity and thermal diffusivity. *Journal of Geophysical Research*, *110*, D15103. https://doi.org/10.1029/2004JD005574

Vadas, S. L., & Fritts, D. C. (2006). Influence of solar variability on gravity wave structure and dissipation in the thermosphere from tropospheric convection. *Journal of Geophysical Research*, *111*, A10S12. https://doi.org/10.1029/2005JA011510

Vadas, S. L., & Fritts, D. C. (2009). Reconstruction of the gravity wave field from convective plumes via ray tracing. *Annales Geophysicae*, *27*, 147–177.

Vadas, S. L., Fritts, D. C., & Alexander, M. J. (2003). Mechanism for the generation of secondary waves in wave breaking regions. *Journal of the Atmospheric Sciences*, *60*, 194–214.

Vadas, S. L., Liu, H.-L., & Lieberman, R. S. (2014). Numerical modeling of the global changes to the thermosphere and ionosphere from the dissipation of gravity waves from deep convection. *Journal of Geophysical Research: Atmospheres*, *119*, 7762–7793. https://doi.org/10.1002/2014JA020280

Vadas, S. L., & Nicolls, M. J. (2009). Temporal evolution of neutral, thermospheric winds and plasma response using PFISR measurements of gravity waves. *Journal of Atmospheric and Solar-Terrestrial Physics*, *71*, 740–770.

Vadas, S. L., & Nicolls, M. J. (2012). The phases and amplitudes of gravity waves propagating and dissipating in the thermosphere: Theory. *Journal of Geophysical Research*, *117*, A05322. https://doi.org/10.1029/2011JA017426

Vadas, S. L., Taylor, M. J., Pautet, P.-D., Stamus, P. A., Fritts, D. C., Liu, H.-L., et al. (2009). Convection: The likely source of medium-scale gravity waves observed in the OH airglow layer near Basilia, Brazil, during the SpreadFEx Campaign. *Annales Geophysicae*, *27*, 231–259.

Vadas, S. L., Zhao, J., Chu, X., & Becker, E. (2018). The excitation of secondary gravity waves from local body forces: Theory and observation. *Journal of Geophysical Research: Atmospheres*, *123*, 9296–9325. https://doi.org/10.1029/2017JD027970

Wu, D. L. (2004). Mesoscale gravity wave variances from AMSU-A radiances. *Geophysical Research Letters*, *28*, L12114. https://doi.org/10.1029/2004GL019562

Wu, D. L., Preusse, P., Eckermann, S. D., Jiang, J. H., Juarez, M. delaT., Coy, L., & Wang, D. Y. (2006). Remote sounding of atmospheric gravity waves with satellite limb and nadir techniques. *Advances in Space Research*, *37*, 2269–2277. https://doi.org/10.1016/j.asr.2005.07.031

Yigit, E., & Medvedev, A. S. (2010). Internal gravity waves in the thermosphere during low and high solar activity: Simulation study. *Journal of Geophysical Research*, *115*, A00G02. https://doi.org/10.1029/2009JA015106